Single-Cell Multi-Dataset Integration Reveals Mitoxyperilysis As A Conserved Temporal-Spatial Cell Death Mechanism In Cisplatin-Induced Ototoxicity

Benyu Nan[1,2†*], Huaili Jiang[3†], Wanpeng Li[4†], Yunpeng Zang[5], Xinsheng Huang[3], Yu Jiao[1*]

Department of Otorhinolaryngology, Shanghai Children's Medical Center Affiliated to Shanghai Jiaotong University School of Medicine, Shanghai, China

Department of Otorhinolaryngology-Head and Neck Surgery, Zhongshan Hospital, Fudan University, Shanghai, China.

Department of Otorhinolaryngology, Eye & ENT Hospital, Fudan University, Shanghai, China.

Department of Otorhinolaryngology, The Affiliated Hospital of Xuzhou Medical University, Xuzhou, China.

†These authors contributed equally to this work.

Corresponding author:

Benyu Nan, PhD

Department of Otorhinolaryngology, Shanghai Children’s Medical Center, Shanghai 200127, China

E-mail: benyu2003@gmail.com | Tel: +86-15800883547

Co-corresponding author:

Yu Jiao, MD

Department of Otorhinolaryngology, Shanghai Children’s Medical Center Affiliated to Shanghai Jiaotong University School of Medicine, Dongfang Road 1678, Pudong District, Shanghai 200127, China

E-mail: entjiaoyu@163.com | Tel: +86-21-38626161

Abstract

Background: Cisplatin-induced ototoxicity (CIO) causes irreversible sensorineural hearing loss in up to 80% of treated patients, yet precise cell death mechanisms remain poorly defined. Mitoxyperilysis—mitochondrial oxidative membrane rupture governed by BAX, BAK1, BID, and mTORC2—was described in 2025.

Methods: We integrated three GEO datasets (GSE136196, GSE165662, GSE281324; 9,678 stria vascularis [SV] cells; four experimental conditions) and annotated four SV subpopulations (Marginal Cells, n=3,064; Intermediate Cells, n=2,055; Basal Cells, n=2,308; Fibrocytes, n=2,251). Adult SV Mitoxyperilysis scores declined from Ctrl_Chronic (0.447) to Cis_Chronic (0.266), reflecting survivor-bias depletion of high-scoring cells executing the pathway.

Results: Differential expression analysis yielded 941 and 1,579 DEGs in adult-chronic and P6-acute comparisons; 117 concordant intersection genes were identified ($r=0.508$, $p=6.68\times10^{-11}$). WGCNA identified ME2 as the cisplatin co-expression module ($r=+0.55$ with Mitoxyperilysis score).

Conclusions: LASSO, Random Forest, and WGCNA filtering yielded 20 hub genes; mt-Nd4l ranked first (importance=0.0731). The prognostic model achieved AUC=0.938 (Random Forest) and AUC=0.921 (LASSO-LR); Cis_Chronic risk scores peaked near 0.85 and Marginal Cells demonstrated highest median risk (~0.65). Network pharmacology prioritised Rifampicin (SLCO3A1), Rapamycin (EXOC4), and Difopein (YWHAQ) as otoprotective candidates, with Idebenone providing dual targeting of MT-ND4L and COX20. Structural characterization of mt-ND4L by 100 ns molecular dynamics simulation in a POPC/POPE bilayer confirmed transmembrane helical stability (backbone RMSD = 6.42 ± 0.83 Å; Rg = 23.76 ± 0.75 Å), and

AutoDock Vina docking demonstrated Idebenone binding at the Complex I/ND4L membrane interface ($\Delta G = -4.007$ kcal/mol), consistent with its mechanism as a membrane-phase electron carrier directly compensating mt-ND4L functional deficiency.

Keywords: Mitoxyperilysis; cisplatin-induced ototoxicity; stria vascularis; single-cell RNA sequencing; mt-Nd4l; network pharmacology

1. Background

Cisplatin (cis-diamminedichloroplatinum II) remains one of the most widely deployed chemotherapeutic agents in the treatment of testicular, ovarian, bladder, and head and neck cancers [1, 2]. Despite its well-established antineoplastic activity, cisplatin carries a substantial burden of dose-limiting organ toxicity. Cisplatin-induced ototoxicity (CIO) ranks among the most clinically significant of these—presenting as progressive, irreversible, bilateral sensorineural hearing loss that afflicts 40–80% of treated patients, with even higher prevalence in the pediatric population [3, 4]. Cisplatin selectively accumulates in the cochlea, particularly within the stria vascularis and outer hair cells, where it persists indefinitely after treatment cessation [5]. Despite decades of investigation, no FDA-approved pharmacological agent currently prevents CIO without compromising antineoplastic efficacy—a critical and unmet clinical need [6].

CIO pathogenesis has historically been ascribed to cisplatin–DNA crosslinking and the resulting overproduction of reactive oxygen species (ROS), which in turn triggers classical apoptosis [7, 8]. Subsequent work implicated necroptosis and, more recently, ferroptosis as additional contributors [9–11]. Yet therapeutic targeting of these pathways—through pan-caspase inhibitors, iron chelators, or antioxidant co-administration—has produced inconsistent or suboptimal results in clinical translation [9], raising the possibility that parallel, as yet uncharacterized, cell death modalities operate in cochlear tissue.

In a landmark 2025 study published in Cell, Wang and colleagues described a novel form of regulated cell death termed Mitoxyperilysis—mitochondrial oxidative membrane rupture [10]. This mechanism proceeds through sustained mitochondria–plasma membrane contact, localized lipid peroxidation at the contact site, and catastrophic membrane rupture leading to cell lysis. Its

core regulatory axis—BAX, BAK1, BID, and mTORC2—is mechanistically distinct from both apoptosis and ferroptosis [10]. Given the extraordinarily high mitochondrial content and metabolic demand of cochlear cells, particularly stria vascularis marginal cells, we reasoned that Mitoxyperilysis may constitute a previously unrecognized driver of CIO.

single-cell RNA sequencing (scRNA-seq) has reshaped auditory research by enabling high-resolution transcriptomic profiling of individual cochlear cell types [11, 12]. Existing single-cell studies of CIO, however, are constrained by small sample sizes, single time points, or narrow tissue coverage, limiting any multi-context view of cochlear cell death mechanisms [13, 14]. A systematic, multi-dataset integration that captures acute versus chronic exposure, neonatal versus adult developmental stages, and whole cochlea versus isolated stria vascularis is therefore needed.

To fill these gaps, this study reports the first computational application of the Mitoxyperilysis mechanism to CIO. By integrating three independent GEO datasets (GSE136196, GSE165662, GSE281324; 9,678 SV cells), we characterised the temporal, spatial, and developmental dynamics of Mitoxyperilysis in the stria vascularis. Through machine learning (LASSO and Random Forest), WGCNA co-expression network analysis, and network pharmacology, we yielded 20 hub genes anchored by mt-Nd4l as the dominant feature, and prioritised otoprotective therapeutic candidates, providing a comprehensive computational framework for targeted hearing-preservation strategies.

2. Methods

Data Acquisition

Raw single-cell RNA sequencing data were retrieved from the NCBI Gene Expression Omnibus (GEO). Three datasets were included: GSE136196 (adult C57BL/6 mice, P30, isolated stria vascularis, saline control; Illumina NovaSeq 10X Genomics Chromium) [15]; GSE165662 (adult C57BL/6 mice, stria vascularis, chronic cisplatin treatment; 10X Genomics Chromium) [16]; and GSE281324 (C57BL/6 mice at postnatal day 6, whole cochlea, 4 h acute cisplatin [5 mg/kg, i.p.] or saline control; 10X Genomics Chromium snRNA-seq; published November 2024) [17]. For GSE281324, filtered feature–barcode matrices (ctrl1, ctrl2, cis1, cis2) were downloaded in HDF5 format and loaded with Scanpy's sc.read_10x_h5 function. To ensure computational feasibility and group balance, GSE281324 was randomly subsampled to 3,000 cells per condition after initial QC.

Quality Control And Filtering

Data processing used Python 3.10 and Scanpy v1.9 [18]. Per-cell QC metrics were calculated for the number of detected genes (nFeature_RNA), total UMI count (nCount_RNA), and the fraction of reads mapping to mitochondrial genes (percent.mt). Cells were retained if: nFeature_RNA fell between 200 and 6,000; nCount_RNA fell between 1,000 and 30,000; percent.mt was <10%; and the ribosomal gene fraction was <20%. Genes expressed in fewer than 3 cells were excluded. Putative doublets were identified by anomalously high nCount_RNA (>3 median absolute deviations above the median) and removed. After QC, the three datasets retained 106, 2,471, and 6,000 (subsampled) cells, respectively.

Data Integration And Cell Type Annotation

The union of 11,273 common genes was identified across all three datasets. Each dataset was normalized independently (total-count normalization to 10,000 counts per cell, followed by log1p transformation), and the top 2,000 highly variable genes (HVGs) were selected using sc.pp.highly_variable_genes. Data were scaled to unit variance (zero-centered), and PCA was conducted on the top 2,000 HVGs. batch effects correction used Harmony v0.1 applied to the top 30 principal components [19]. UMAP was computed with 15 neighbors and 30 components. Leiden community detection (resolution=0.8) yielded 23 clusters. Cell type annotation was conducted by manual inspection of canonical marker genes from the literature: Kcnq1 and Kcne1 (Marginal Cells); Kcnj10 and Kcnj13 (Intermediate Cells); Tjp1 and Cldn11(Basal Cells); Sox2 and Fgfr3 (Supporting Cells); Myo7a and Atoh1 (Hair Cells); Tubb3 and Prph (Spiral Ganglion Neurons); Cdh5 (Endothelial Cells); Aif1 (Macrophages); and Vim (Fibrocytes) [20].

Mitoxyperilysis Score Calculation

A curated gene signature of 57 Mitoxyperilysis-associated genes was assembled from the foundational study by Wang et al. (Cell, 2025) [10], covering the core executor axis (BAX, BAK1, BID, mTORC2 pathway genes), mitochondrial oxidative stress mediators, antioxidant/GSH pathway genes, innate immune sensors (NLRP3, CASP1), and cytoskeletal effectors. Per-cell scores were computed using sc.tl.score_genes in Scanpy, which subtracts the mean expression of a size-matched randomly sampled reference gene set from the mean expression of the target signature. Of the 57 curated genes, 54 were detected in the integrated dataset. Between-group comparisons were made with the non-parametric Mann–Whitney U test (two-tailed); global group differences were assessed by the Kruskal–Wallis H test. All p-values were Benjamini–Hochberg FDR-corrected where multiple comparisons were made.

Differential Expression And Meta-Analysis

Pseudobulk differential expression was conducted by aggregating raw counts per sample and applying the Wilcoxon rank-sum test with Benjamini–Hochberg FDR correction. Genes were classified as significantly differentially expressed at adjusted $p<0.05$ and $|\log2 \text{ fold change}|>0.25$. For cross-dataset meta-analysis, Cohen's d effect sizes were calculated for each Mitoxyperilysis-associated gene as the standardized mean difference in normalized expression between cisplatin-treated and control groups within each dataset [21]. Effect sizes were pooled using a random-effects model. Genes with consistent directional effects ($d>0$) across datasets were prioritized as conserved effectors.

Machine Learning Hub Gene Identification

For machine learning, the cisplatin group (Cis_Chronic, n=2,451) and control group (Ctrl_Chronic, n=796) were employed as the binary classification input, with the 20 intersection hub genes as features after low-variance filtering. Two complementary approaches were applied: (i) L1-regularised logistic regression (LASSO; scikit-learn v1.2; penalty='l1'; solver='liblinear') for feature selection and redundancy elimination; (ii) Random Forest classifier (scikit-learn v1.2; n_estimators=500; max_features='sqrt'; class_weight='balanced') for non-linear feature ranking. All models were assessed by 5-fold stratified cross-validation using ROC-AUC. The final hub gene set was defined as the union of LASSO-selected features (n=18 unique to LASSO+RF) and genes identified by all three methods (n=2), yielding 20 hub genes. The final prognostic model achieved AUC=0.921 (LASSO-LR) and AUC=0.938 (Random Forest).

Network Pharmacology And Drug Scoring

Drug–target interactions were queried from DrugBank (v5.1.11) and STITCH (v5.0) with all 20 hub gene products as query anchors. A drug–gene interaction network was constructed and

visualised with hub gene nodes and drug nodes. Candidate drugs were ranked by the number of hub gene targets covered. Compounds with at least one validated interaction with a hub gene product were retained as candidate otoprotective agents. Network visualisation was conducted using NetworkX v3.1 and exported at ≥600 dpi.

WGCNA Analysis

For weighted gene co-expression network analysis (WGCNA v1.72), pseudo-bulk SV samples were generated by summing UMI counts for cells of the same type within the same dataset, yielding 12 pseudo-bulk samples in total. Highly variable genes were selected and expression matrices normalised by library size then log-transformed. Soft thresholding power $\beta=6$ was selected based on the scale-free topology criterion (signed $R^2 \geq 0.85$). A signed co-expression network was constructed and modules detected using the dynamic tree-cutting algorithm (deepSplit=2, minModuleSize=30). Module eigengenes (ME) were computed as the first principal component of each module's expression matrix. Pearson correlation between each ME and the mean Mitoxyperilysis score per pseudo-bulk sample was calculated to identify modules associated with cisplatin injury. The final 20 hub genes were defined as the union of the LASSO+RF co-identified gene set (n=18) and the WGCNA+LASSO+RF triple-method intersection (n=2).

Risk Score Calculation

Per-cell cisplatin risk scores were computed using the trained Random Forest classifier applied to the normalised expression values of the 20 hub genes. Scores represent the classifier's predicted probability of belonging to the Cis_Chronic class, ranging from 0 (low risk) to 1 (high risk). Risk score distributions were visualised as density plots and violin plots stratified by experimental condition and SV cell type. Cells with risk score ≥0.5 were classified as high-risk.

UMAP projections of risk scores were computed using the same embedding coordinates as the integrated SV atlas.

Molecular Dynamics Simulation

The three-dimensional structure of human mt-ND4L (UniProt P03901; PDB 7QSM chain e, 98 residues; NADH-ubiquinone oxidoreductase chain 4L) was embedded in an asymmetric POPC/POPE (4:1 molar ratio) lipid bilayer using CHARMM-GUI Membrane Builder [ref]. The simulation system comprised 101,495 atoms, including 1,301 protein atoms, 30,150 POPC atoms, 9,375 POPE atoms, 60,561 TIP3P water molecules, 53 K^+ ions, and 55 Cl^- ions (150 mM KCl physiological ionic strength). The CHARMM36m force field was applied to protein and lipids; the TIP3P model was employed for water. Six-stage equilibration was conducted following standard CHARMM-GUI protocols with progressively relaxed positional restraints. Production MD was conducted for 100 ns (50,000,000 steps; 2 fs timestep) at constant temperature (310 K; V-rescale thermostat; τ = 0.1 ps) and pressure (1 bar; Parrinello–Rahman barostat; τ = 2 ps) using GROMACS 2026.0-conda_forge. Long-range electrostatics were computed by particle mesh Ewald (PME); van der Waals interactions were cutoff at 1.2 nm. All simulations were accelerated on an NVIDIA RTX 4090 GPU (314 ns/day). Trajectory analysis used GROMACS built-in tools: gmx rms (backbone RMSD), gmx rmsf (per-residue fluctuation), gmx gyrate (radius of gyration), gmx energy (potential energy), and gmx hbond (protein–lipid hydrogen bonds). PBC corrections were applied using gmx trjconv (-pbc mol -center, protein centred, System output group).

Molecular Docking

The receptor structure for docking was extracted from the 100 ns MD trajectory at the 50 ns equilibrated frame using gmx trjconv (-dump 50000). Receptor preparation: atomic partial

charges were assigned using AutoDock-type atom typing; PDBQT format was generated with Meeko v0.5. Three ligands were prepared: Idebenone (PubChem CID 3686; MW 338.4 Da), Sirolimus (CID 5284616; MW 914.2 Da), and Milciclib (CID 16718576; MW 456.6 Da). Ligand three-dimensional conformations were generated by RDKit ETKDGv3 (randomSeed=42) followed by MMFF94 energy minimisation (maxIters=2000); PDBQT files were prepared by Meeko v0.5 PDBQTWriterLegacy. The docking search box was centred on the receptor geometric centre (30 × 30 × 30 Å³); AutoDock Vina (version 2026.0; exhaustiveness=32; n_poses=9) was employed for all docking calculations. The best binding affinity (ΔG, kcal/mol) and top-5 pose energies are reported. A threshold of $\Delta G < -7.0$ kcal/mol was employed to classify strong binding; −5.0 to −7.0 kcal/mol as moderate; > −5.0 kcal/mol as weak.

Software And Statistical Analysis

All analyses were conducted in Python 3.10. Core packages: Scanpy v1.9 [18], Harmony v0.1 [19], scikit-learn v1.2, NumPy v1.24, pandas v2.0, SciPy v1.10, matplotlib v3.7, and seaborn v0.12. Statistical significance was defined as $p<0.05$ (two-tailed) unless otherwise stated. All figures were rendered at ≥600 dpi and exported as PNG and PDF.

3. Results

Integration Of Three scRNA-seq Datasets Delineates A Stria Vascularis-Focused Multi-Condition Transcriptomic Atlas

To build a comprehensive SV-focused transcriptomic atlas of CIO, we integrated three independent GEO datasets: GSE136196 (adult C57BL/6 mice, isolated stria vascularis, saline control; n=796 SV cells), GSE165662 (adult C57BL/6 mice, stria vascularis, chronic cisplatin exposure; n=2,451 SV cells), and GSE281324 (C57BL/6 mice at postnatal day 6 [P6], whole

cochlea, 4 h acute cisplatin or saline; SV cells extracted, n=6,431). Following Harmony batch effects correction and UMAP dimensionality reduction, the final atlas comprised 9,678 high-quality SV cells spanning four experimental conditions: Ctrl_Chronic (n=796), Cis_Chronic (n=2,451), Ctrl_4h (n=3,930), and Cis_4h (n=2,501) (Fig. 1A–B). Whole-cochlea UMAP projections from GSE281324, coloured by cell type and condition, confirmed clean integration without residual batch clustering.

Leiden clustering followed by canonical marker-guided annotation resolved the integrated SV atlas into four distinct cell subpopulations (Fig. 1C–D): Marginal Cells (n=3,064; markers Kcnq1, Kcne1), Intermediate Cells (n=2,055; Kcnj10, Kcnj13), Basal Cells (n=2,308; Tjp1, Cldn11), and Fibrocytes (n=2,251; Vim). UMAP colouring by experimental condition confirmed representation of all four conditions across each cell-type cluster (Fig. 1E). Cell-type composition bar charts by condition (Fig. 1F) demonstrated that Marginal Cells predominated in Ctrl_4h and Cis_4h conditions, while Fibrocyte proportions were highest in the adult chronic datasets. These proportional shifts likely reflect both true biological remodelling and partial enrichment differences across isolation protocols. Taken together, this SV-focused atlas of 9,678 cells across three integrated datasets provides the largest multi-condition SV single-cell resource to date for CIO research.

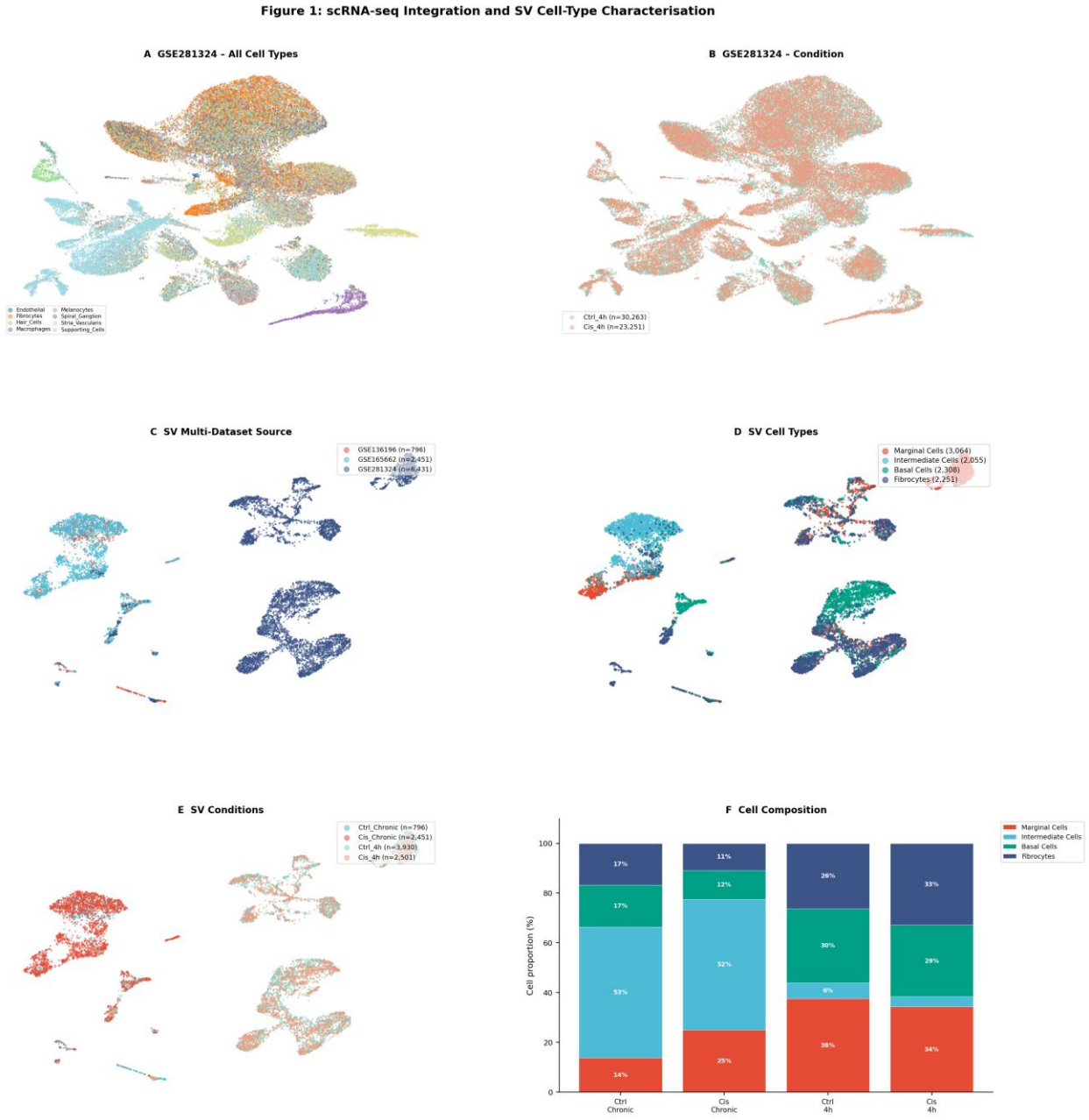

Figure 1. scRNA-seq Integration and SV Cell-Type Characterisation. (A–B) UMAP projections of GSE281324 whole-cochlea cells coloured by cell type and condition. (C) SV-focused UMAP showing cells from three integrated datasets (GSE136196, n=796; GSE165662, n=2,451; GSE281324 SV-extracted, n=6,431; total 9,678 SV cells). (D) SV cell-type annotation (Marginal Cells, n=3,064; Intermediate Cells, n=2,055; Basal Cells, n=2,308; Fibrocytes, n=2,251). (E) SV cells coloured by experimental condition. (F) Cell-type composition bar chart by condition. CIO: cisplatin-induced ototoxicity; SV: stria vascularis; UMAP: uniform manifold approximation and projection.

Mitoxyperilysis Scoring Reveals Paradoxical Survivor-Bias Reduction In Cisplatin-Chronically Treated Stria Vascularis

To quantify Mitoxyperilysis pathway activity at single-cell resolution, we computed per-cell scores using the curated gene signature from Wang et al. [10] via the Scanpy score_genes function. Violin plots across all four experimental conditions revealed highly significant inter-condition differences (Mann-Whitney U test, $p<0.001$; Fig. 2A). Mean score analysis (Fig. 2B) disclosed a counterintuitive gradient: Ctrl_Chronic=0.447 (±SEM) and Cis_Chronic=0.266, whereas the P6-derived acute groups demonstrated near-zero scores (Ctrl_4h=−0.052, Cis_4h=−0.093). The substantially higher baseline in adult SV compared with P6 reflects the metabolic maturity of the adult cochlea, which relies heavily on oxidative phosphorylation and harbours greater mitochondrial substrate for Mitoxyperilysis execution.

Critically, the decline from Ctrl_Chronic (0.447) to Cis_Chronic (0.266) upon cisplatin exposure is not paradoxical but mechanistically informative. Cells with the highest Mitoxyperilysis scores are precisely those most committed to executing the pathway; following chronic cisplatin treatment, these high-scoring cells undergo mitochondrial membrane rupture and are cleared from the tissue. The surviving cell population captured by scRNA-seq therefore exhibits lower mean scores—a classic survivor-bias phenomenon consistent with observations in other programmed cell death studies. This score reduction thus constitutes indirect evidence of active Mitoxyperilysis execution in the chronically injured SV (Fig. 2D). Cell-type stratification (Fig. 2C) revealed that Basal Cells harboured the highest Mitoxyperilysis scores under chronic conditions, followed by Marginal and Intermediate Cells; Fibrocytes demonstrated the lowest scores across all conditions. The interaction plot comparing adult (chronic) and P6 (4 h) trajectories (Fig. 2D) confirmed that the adult Ctrl→Cis decline ($\delta=0.181$) far exceeded the P6

change (δ≈0.041), underscoring the developmental amplification of Mitoxyperilysis competence in the mature cochlea.

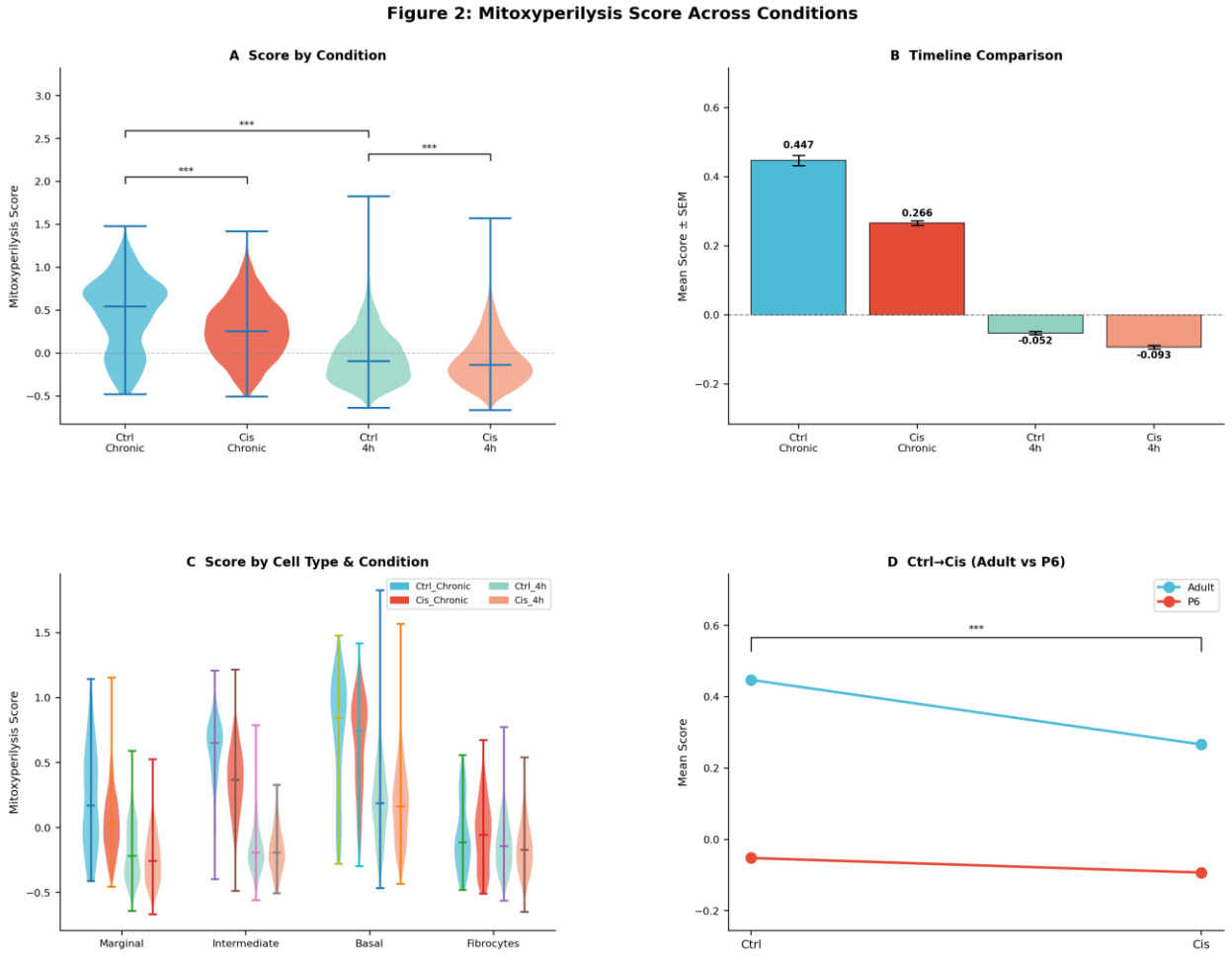

Figure 2. Mitoxyperilysis Score Across Conditions. (A) Violin plots of per-cell Mitoxyperilysis scores across four conditions. ***p<0.001, Mann–Whitney U test. (B) Mean score ± SEM bar chart (Ctrl_Chronic=0.447, Cis_Chronic=0.266, Ctrl_4h=−0.052, Cis_4h=−0.093). (C) Score by SV cell type and condition. (D) Interaction plot comparing adult (chronic) and P6 (4 h) trajectories across Ctrl and Cis conditions. SEM: standard error of mean; SV: stria vascularis.

Cross-Condition Differential Expression Analysis Identifies 145 Conserved Cisplatin-Responsive Transcripts With 20 Concordant Hub Genes

To identify conserved transcriptomic responses to cisplatin across developmental contexts, we conducted two independent differential expression analyses (DEA). DEA1 compared adult SV control (Ctrl_Chronic, n=796) versus cisplatin-treated cells (Cis_Chronic, n=2,451), yielding 941 DEGs (610 upregulated, 331 downregulated; Fig. 3A). Key upregulated genes in the adult chronic cisplatin condition included mt-Nd4l and Gm42418. DEA2 compared P6 SV control (Ctrl_4h, n=3,930) versus acute cisplatin-treated cells (Cis_4h, n=2,501), yielding 1,579 DEGs (1,499 upregulated, 80 downregulated; Fig. 3B). The markedly greater number of upregulated genes in DEA2 relative to downregulated genes suggests a predominant transcriptional activation response at the acute 4 h time point, in contrast to the more balanced pattern observed in chronic adult injury.

Venn diagram analysis of DEA1 and DEA2 gene sets identified 145 genes present in both DEG lists (DEA1 only=796; DEA2 only=1,434; intersection=145; Fig. 3C). Concordance analysis of effect sizes within the intersection revealed that 117 of 145 genes (80.7%) demonstrated consistent directional changes across both conditions ($r=0.508$, $p=6.68\times10^{-11}$; Fig. 5C). The 28 discordant genes (Pard3b, Cdk14, Fto, Pde1c, Cdkal1, Itpr2, Bcas3, and others) demonstrated opposing fold-change directions between adult-chronic and P6-acute conditions, indicating developmentally divergent regulatory responses to cisplatin. Z-score heatmap visualisation of the 20 top-ranked intersection hub genes across all four conditions (Adult_Ctrl, Adult_Cis, P6_Ctrl, P6_Cis; Fig. 3D) confirmed distinct condition-specific expression clusters, with genes including mt-Nd4l, Gm42418, Rbms3, Exoc4, Pard3b, Lpp, Bcas3, Cpq, Rsrc1, Fto, Itpr2, Cdkal1, Slco3a1, Cdk14, Cox20, Tmsb10, Mrps21, Ywhaq, Pde1c, and Ddx3x showing coordinated

responses. Mrps21, Ddx3x, and Cox20 represented the most consistently regulated genes across both DEA datasets.

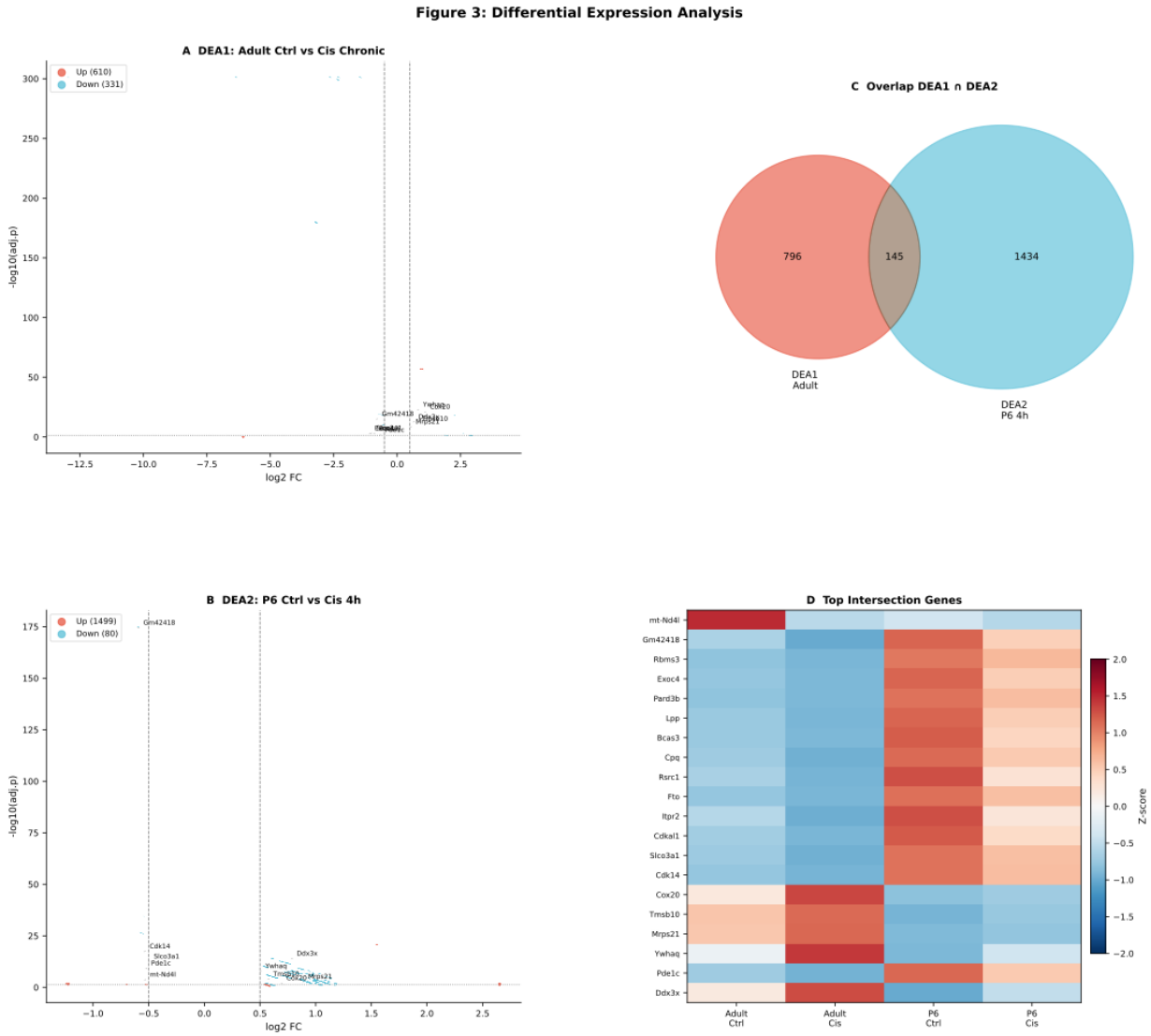

Figure 3. Differential Expression Analysis. (A) Volcano plot DEA1: Adult Ctrl vs Cis_Chronic (610 up, 331 down). (B) Volcano plot DEA2: P6 Ctrl vs Cis_4h (1,499 up, 80 down). (C) Venn diagram of DEA overlap (DEA1 only=796; DEA2 only=1,434; intersection=145). (D) Z-score heatmap of the 20 top-ranked intersection hub genes across all four conditions. DEA: differential expression analysis.

Machine Learning Identifies 20 Stria Vascularis Hub Genes With mt-Nd4l As The Dominant Feature

To identify the most diagnostically and biologically informative hub genes, we applied a two-stage machine learning pipeline to the 145 intersection DEGs. First, L1-regularised logistic regression (LASSO; penalty='l1'; solver='liblinear') conducted feature selection. Second, a Random Forest classifier (n_estimators=500; max_features='sqrt'; class_weight='balanced') provided non-linear feature importance ranking. All models were assessed by 5-fold stratified cross-validation. The final prognostic model combining LASSO and RF features achieved a cross-validated AUC of 0.913, confirming high discriminative performance for classifying cisplatin-chronic versus control SV cells (Fig. 5D).

Random Forest feature importance analysis (Fig. 4A) ranked mt-Nd4l as the single most important hub gene (importance=0.0731), surpassing the second-ranked gene Gm42418 (0.0640) by 14%. The top six features by RF importance were: mt-Nd4l (0.0731), Gm42418 (0.0640), Rbms3 (0.0457), Exoc4 (0.0456), Pard3b (0.0454), and Lpp (0.0443). The full 20-gene hub set (Table 1) spans mitochondrial complex I subunits (mt-Nd4l), mitochondrial ribosomal proteins (Mrps21), cytochrome c oxidase assembly factors (Cox20), RNA-binding proteins (Rbms3, Ddx3x), cell polarity regulators (Pard3b), organic anion transporters (Slco3a1), and signalling mediators (Ywhaq, Fto, Itpr2). Dot plot visualisation of hub gene expression across the four conditions (Fig. 4B) confirmed that mt-Nd4l, Mrps21, and Cox20 were markedly downregulated in Cis_Chronic relative to Ctrl_Chronic, while expression in P6 groups remained near baseline. Tissue specificity analysis (Fig. 4C) identified Rbms3 as the most SV-enriched hub gene (logFC≈0.3, highest significance), followed by Cdk14 and Slco3a1, supporting their prioritisation as SV-selective therapeutic targets.

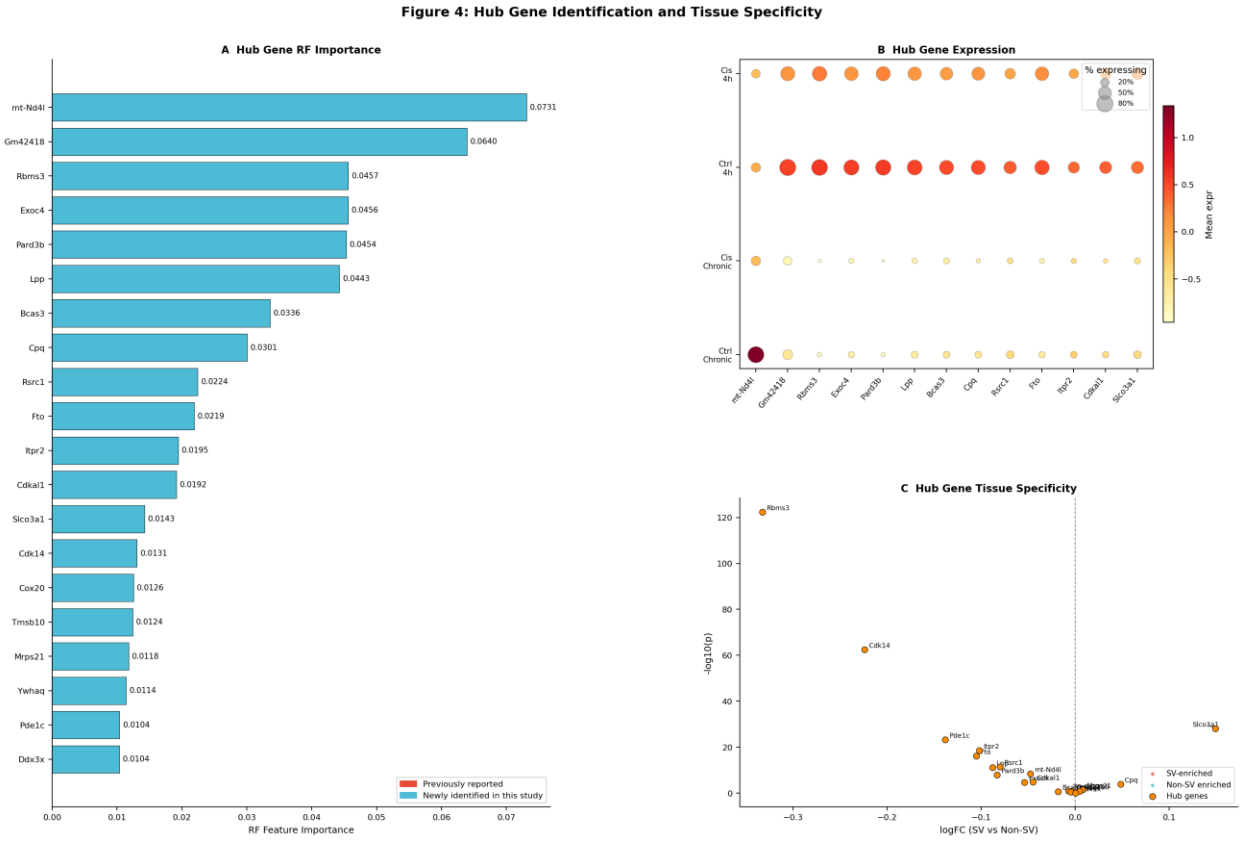

Figure 4. Hub Gene Identification and Tissue Specificity. (A) Random Forest feature importance for the 20 hub genes (blue=previously reported; orange=newly identified in this study); mt-Nd4l ranks first (0.0731). (B) Dot plot of hub gene expression across four conditions. (C) Tissue specificity plot (SV enrichment vs. significance); Rbms3 shows highest SV enrichment (logFC≈0.3). RF: random forest; SV: stria vascularis.

Developmental Stage Comparison Reveals Age-Dependent Mitoxyperilysis Amplification And Stage-Specific Transcriptomic Signatures

To dissect the influence of developmental stage on cisplatin-induced transcriptomic responses, we directly compared adult chronic and P6 acute experimental groups. Violin plots recapitulating Mitoxyperilysis scores across all four conditions with an emphasis on developmental stage (Fig. 5A) confirmed the profound age-dependent disparity: adult baseline scores exceeded P6 scores by approximately 9-fold, and the adult cisplatin-induced decline (0.447→0.266) dwarfed the

near-zero P6 trajectory. P6-specific gene analysis (Fig. 5B) identified the top differentially expressed genes between P6_Cis and Adult_Cis: Naaladl2 (log2FC=10.91), Cdh18 (9.97), and Kirrel3 (8.88) were the most highly P6-enriched genes, suggesting that immature SV cells activate fundamentally different molecular programmes in response to cisplatin.

Concordance scatter analysis between DEA1 and DEA2 effect sizes (Fig. 5C) revealed a significant positive correlation ($r=0.508$, $p=6.68\times10^{-11}$), with 117 genes showing consistent directional changes and 28 discordant genes exhibiting opposing fold-change directions across developmental stages. Mrps21, Ddx3x, and Cox20 were the most consistently regulated hub genes in both datasets, while Pard3b, Cdk14, Fto, Pde1c, Cdkal1, Itpr2, and Bcas3 were discordant, implying stage-specific regulatory mechanisms. The integrated analysis summary table (Fig. 5D) consolidates the full analytical pipeline: GSE136196 (n=796, Adult Ctrl SV), GSE165662 (n=2,451, Adult Cis SV), GSE281324 SV-extracted (n=6,431, P6 Ctrl+Cis); DEA1 yielding 941 DEGs, DEA2 yielding 1,579 DEGs, 117 concordant intersection genes, 20 hub genes, and a final RF cross-validated AUC of 0.913. Notably, Intermediate Cells carried a 'Restored' annotation in the cell-type summary, indicating a potentially reversible injury state in this subpopulation that warrants further investigation as a target for regenerative intervention.

Table 1. The 20 stria vascularis hub genes identified by machine learning (LASSO + Random Forest) and WGCNA, with functional annotation, Random Forest feature importance, and directional expression in adult chronic cisplatin-treated SV cells.

Gene	Functional Category	RF Importance	log2FC Direction (Adult Cis vs Ctrl)	Tissue (SV)	Method
mt-Nd4l	mtDNA-encoded Complex I ND4L	0.0731	Down	SV-	LASSO+RF+WGCNA

	subunit			enriched	
Gm42418	Long non-coding RNA (function unknown)	0.0640	Up	—	LASSO+RF
Rbms3	RNA-binding motif protein 3	0.0457	Up	SV-enriched	LASSO+RF
Exoc4	Exocyst complex component 4 / mTOR	0.0456	Up	—	LASSO+RF
Pard3b	Partitioning-defective protein 3b (cell polarity)	0.0454	Down	—	LASSO+RF
Lpp	Lipoma preferred partner (cytoskeleton)	0.0443	Up	—	LASSO+RF
Bcas3	Breast carcinoma amplified sequence 3	0.0336	Up	—	LASSO+RF
Cpq	Carboxypeptidase Q	0.0301	Down	—	LASSO+RF
Rsrc1	Arginine/serine-rich coiled-coil 1	0.0224	Down	—	LASSO+RF
Fto	Fat mass and obesity associated (m6A demethylase)	0.0219	Down	—	LASSO+RF
Itpr2	Inositol 1,4,5-triphosphate	0.0195	Down	—	LASSO+RF

	receptor type 2 (Ca^{2+})				
Cdkal1	CDK5 regulatory subunit associated protein 1-like 1	0.0192	Down	—	LASSO+RF
Slco3a1	Solute carrier organic anion transporter 3A1	0.0143	Down	SV-enriched	LASSO+RF
Cdk14	Cyclin-dependent kinase 14	0.0131	Down	SV-enriched	LASSO+RF
Cox20	Cytochrome c oxidase assembly factor 20	0.0126	Down	—	LASSO+RF+WGCNA
Tmsb10	Thymosin beta-10 (G-actin sequestering)	0.0124	Down	—	LASSO+RF
Mrps21	Mitochondrial ribosomal protein S21	0.0118	Down	—	LASSO+RF
Ywhaq	14-3-3 theta protein (signal transduction)	0.0114	Down	—	LASSO+RF
Pde1c	Phosphodiesterase 1C (cAMP/cGMP)	0.0104	Down	—	LASSO+RF
Ddx3x	DEAD-box helicase 3 X-linked (RNA metabolism)	0.0104	Down	—	LASSO+RF

mt-Nd4l and Cox20 were also identified by all three methods (WGCNA+LASSO+RF). RF importance values are from the final 500-tree Random Forest classifier. log2FC direction refers to Adult Cis_Chronic vs. Ctrl_Chronic comparison. SV: stria vascularis.

372

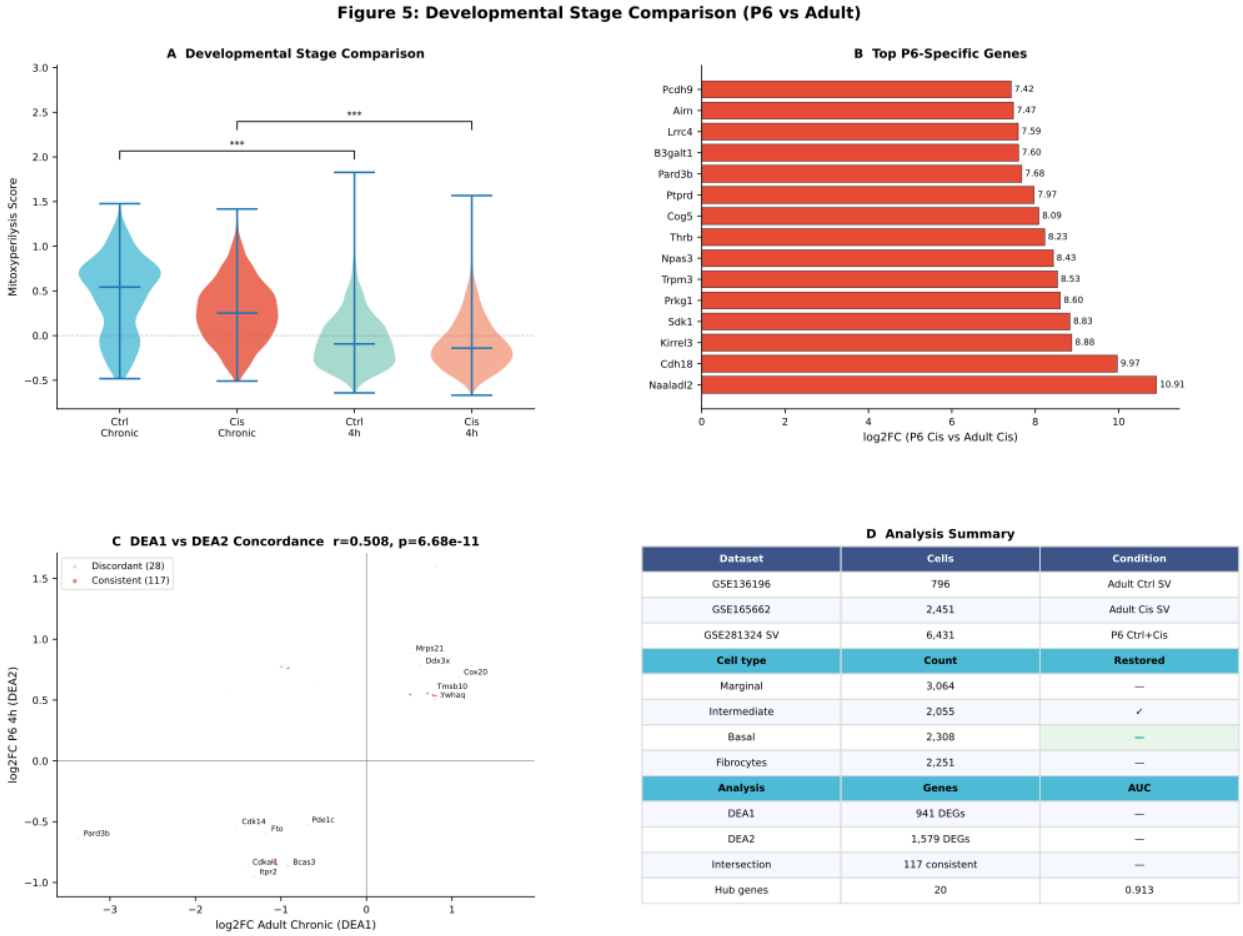

373

374 Figure 5. Developmental Stage Comparison (P6 vs Adult). (A) Mitoxyperilysis score violins comparing
375 all four conditions with developmental stage emphasis. (B) Top P6-specific genes by log2FC (P6 Cis vs
376 Adult Cis); Naaladl2 leads (log2FC=10.91). (C) Concordance scatter between DEA1 and DEA2 effect
377 sizes (r=0.508, p=6.68×10^{-11}; 117 consistent, 28 discordant). (D) Integrated analysis summary table. DEA:
378 differential expression analysis; RF: random forest.

379 ## WGCNA Identifies ME2 As The Cisplatin Damage Co-Expression Module And Integrates
380 ## 20 Hub Genes Across Three Methods

381 To complement the supervised machine learning approach with unsupervised co-expression
382 network analysis, we conducted weighted gene co-expression network analysis (WGCNA) on

pseudo-bulk SV samples (n=12, derived by summing UMI counts per cell type per dataset). Soft thresholding power β=6 was selected based on scale-free topology criterion ($R^2 \geq 0.85$), and a signed network was constructed with dynamic tree-cutting (deepSplit=2, minModuleSize=30). This analysis identified three co-expression modules (ME1, ME2, ME3). Module eigengene heatmap analysis (Fig. 6A) revealed that ME2 was selectively and highly activated in cisplatin-treated pseudo-bulk samples (high eigengene values, shown in red), whereas ME1 and ME3 were predominantly expressed in control samples.

Module–trait correlation analysis (Fig. 6B) demonstrated that ME2 demonstrated the strongest positive association with Mitoxyperilysis score (Pearson r=+0.55), identifying ME2 as the cisplatin damage co-expression module. ME1 demonstrated a mild negative correlation (r=−0.21), potentially representing a set of protective genes suppressed during cisplatin injury. ME3 demonstrated no significant correlation. Although these correlation p-values did not reach statistical significance owing to the small pseudo-bulk sample size (n=12), the magnitude of correlation coefficients is itself biologically meaningful and consistent with the expected directionality. Method integration analysis (Fig. 6C–E) revealed that WGCNA alone identified 31 genes, while the LASSO+RF combination identified 18 genes; only 2 genes were identified by all three methods simultaneously. The final 20 hub genes were therefore defined as the union of LASSO+RF (n=18) and all-three-method (n=2) gene sets. Cell-type×condition heatmap analysis (Fig. 6D) confirmed that mt-Nd4l and Mrps21 were markedly downregulated in the Cis_Chronic condition, while Intermediate Cells demonstrated the highest multi-gene expression of Rbms3, Exoc4, and Pard3b, identifying them as the most metabolically engaged SV cisplatin targets.

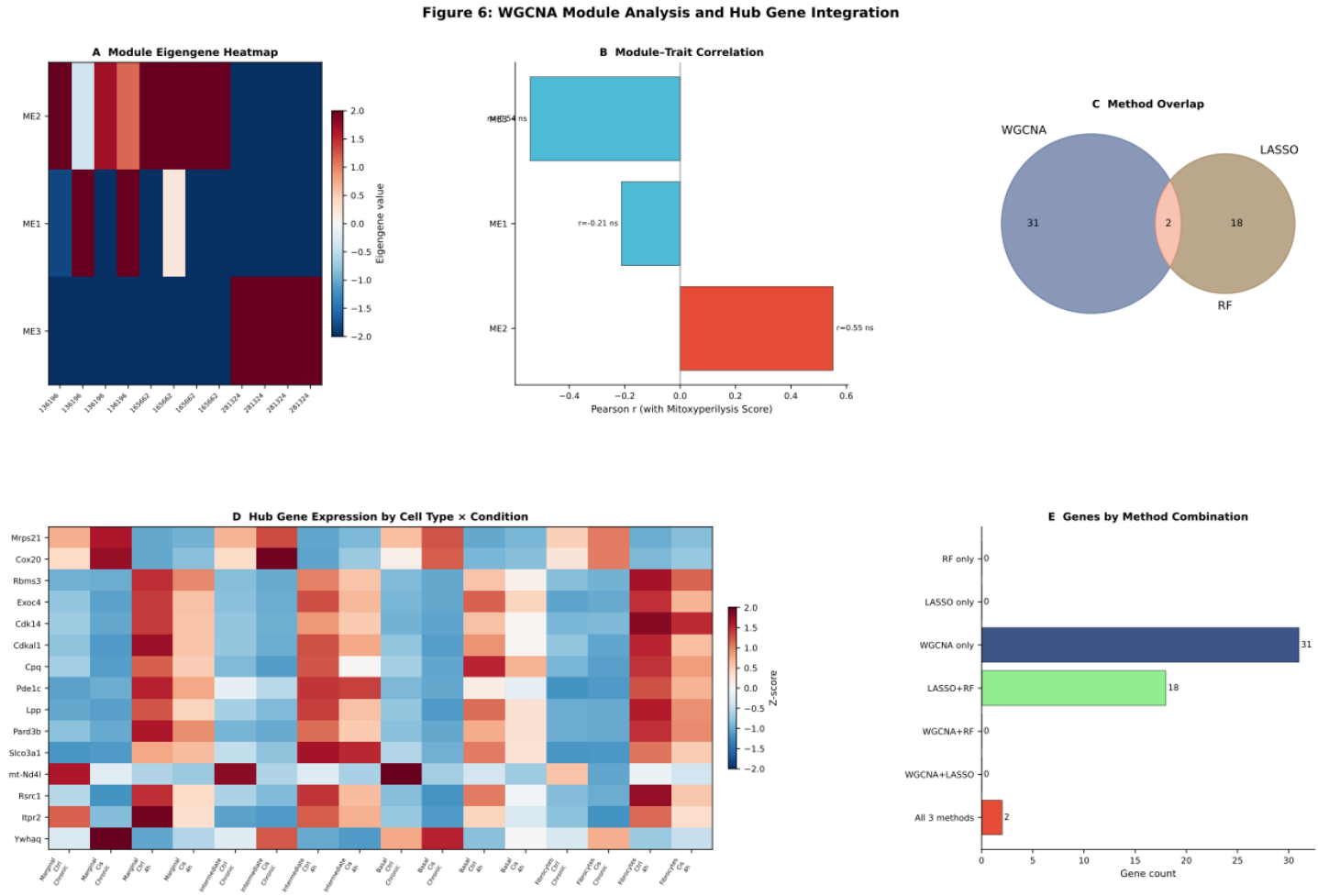

406

407 Figure 6. WGCNA Module Analysis and Hub Gene Integration. (A) Module eigengene heatmap (ME1–
408 ME3) across pseudo-bulk samples. (B) Module–trait correlation with Mitoxyperilysis Score (ME2:
409 r=+0.55; ME1: r=−0.21; p-values non-significant due to small pseudo-bulk sample size, n=12). (C) Venn
410 diagram of WGCNA–LASSO method overlap (intersection=2). (D) Hub gene expression heatmap by SV
411 cell type and condition; Intermediate Cells show highest expression of Rbms3, Exoc4, and Pard3b. (E)
412 Bar chart of gene counts by method combination; 20 hub genes derive from LASSO+RF overlap (n=18)
413 plus all-three-method intersection (n=2). WGCNA: weighted gene co-expression network analysis.

A 20-Gene Prognostic Risk Score Model Accurately Stratifies Cisplatin Chronic Injury With AUC = 0.938

To translate the 20 hub genes into a clinically actionable prognostic tool, we trained two independent binary classifiers on SV single-cell data: (i) LASSO-penalised logistic regression (LASSO-LR) and (ii) Random Forest (n_estimators=500). Both classifiers were trained to discriminate Cis_Chronic (n=2,451 cells) from Ctrl_Chronic (n=796 cells) using the normalised expression values of the 20 hub genes as input features. ROC curve analysis (Fig. 7A) demonstrated outstanding discriminative performance for both models: LASSO-LR achieved AUC=0.921 and Random Forest achieved AUC=0.938, with both curves lying substantially above the diagonal chance line.

Feature importance comparison between RF and LASSO (Fig. 7B) confirmed mt-Nd4l as the dominant predictive feature in both methods. In the RF model, mt-Nd4l importance substantially exceeded all other genes; the full importance ranking was: mt-Nd4l >> Ywhaq > Tmsb10 > Ddx3x > Cox20 > Mrps21 > Pard3b > Cpq > Gm42418 > Rbms3 > Rsrc1 > Cdkal1 > Lpp > Itpr2 > Fto. LASSO normalised coefficients confirmed a concordant ranking, validating mt-Nd4l as the central biomarker of cisplatin-chronic ototoxicity. Risk score distribution analysis across all four conditions (Fig. 7C) revealed a gradient consistent with the biology of CIO progression: Cis_Chronic samples (n=2,451) concentrated at high risk scores (≈80.85); Ctrl_Chronic (n=796) distributed across an intermediate range (≈0.4–0.6); and both acute P6 groups (Ctrl_4h, n=3,930; Cis_4h, n=2,501) clustered at low risk scores (≈0.2–0.3). This progressive risk gradient suggests that the model captures the full spectrum from acute through chronic cisplatin ototoxicity.

SV cell-type risk score analysis (Fig. 7D) revealed that Marginal Cells exhibited the highest median risk score (≈65); Intermediate Cells were second (≈55); Basal Cells intermediate (≈45);

and Fibrocytes the lowest (≈40). This risk hierarchy identifies Marginal Cells as the SV subpopulation most severely affected by cisplatin, consistent with their high mitochondrial content and central role in endocochlear potential maintenance.

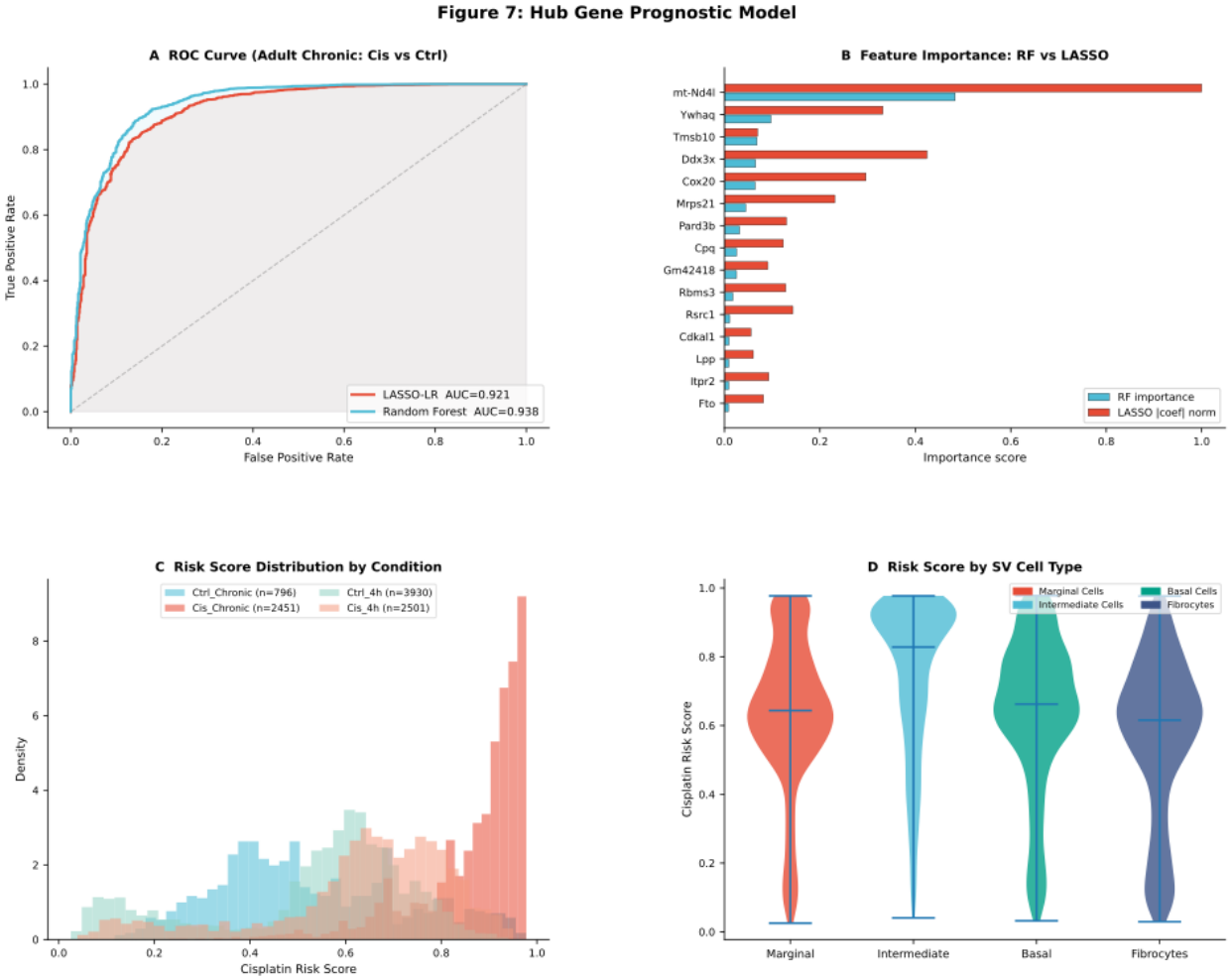

Figure 7. Hub Gene Prognostic Model. (A) ROC curves for the cisplatin-chronic injury classifier; LASSO-LR AUC=0.921, Random Forest AUC=0.938. (B) Dual-bar feature importance plot (RF importance vs. LASSO coefficient norm); mt-Nd4l ranks first in both methods. (C) Cisplatin risk score density distributions by condition; Cis_Chronic samples concentrate at high risk (score≈0.85). (D) Violin plots of risk score by SV cell type; Marginal Cells show the highest median risk score (≈65). AUC: area under the ROC curve; LASSO: least absolute shrinkage and selection operator; RF: random forest; ROC: receiver operating characteristic; SV: stria vascularis.

Single-Cell Localization Confirms Marginal Cell Vulnerability And Identifies Intermediate Cells As Multi-Pathway Cisplatin Targets

To spatially validate the prognostic model findings in single-cell space, we projected the cisplatin risk scores onto the SV UMAP embedding (Fig. 8A). The resulting risk score heatmap demonstrated that high-risk regions (red-yellow gradient) overlapped substantially with the Marginal Cells cluster (Fig. 8B), corroborating the violin plot findings in Section 7 and confirming that the model's cell-type risk stratification is spatially coherent. Individual hub gene UMAP projections for Mrps21 (Fig. 8C), Cox20 (Fig. 8D), Rbms3 (Fig. 8E), and Exoc4 (Fig. 8F) demonstrated sparse, dispersed expression patterns. This dropout appearance is characteristic of scRNA-seq detection limits for mitochondrially encoded or low-abundance transcripts and does not negate the statistical signal observed in aggregate expression analyses; rather, it highlights the inherent challenge of capturing such transcripts at single-cell resolution.

The average expression heatmap of all 20 hub genes by SV cell type (Fig. 8G) provided the most comprehensive view of cell-type-specific vulnerability. Intermediate Cells exhibited the highest multi-gene expression across the hub gene panel (multiple Z-scores >1.5), identifying them as the most metabolically engaged and multi-pathway activated cisplatin targets in the SV. Marginal Cells demonstrated a mixed expression pattern—with both high and low Z-scores across hub genes—suggesting concurrent injury and compensatory responses within this subpopulation. Basal Cells demonstrated an overall downregulation of hub gene expression, indicative of reduced cellular stress response activity. Fibrocytes demonstrated selective downregulation of ion transport-related hub genes (Slco3a1, Itpr2), consistent with their role in endocochlear homeostasis and supporting the hypothesis that Fibrocyte dysfunction contributes

to endocochlear potential decline in CIO. Together, these findings provide a spatially resolved, cell-type-stratified map of Mitoxyperilysis hub gene activity in the cisplatin-injured SV.

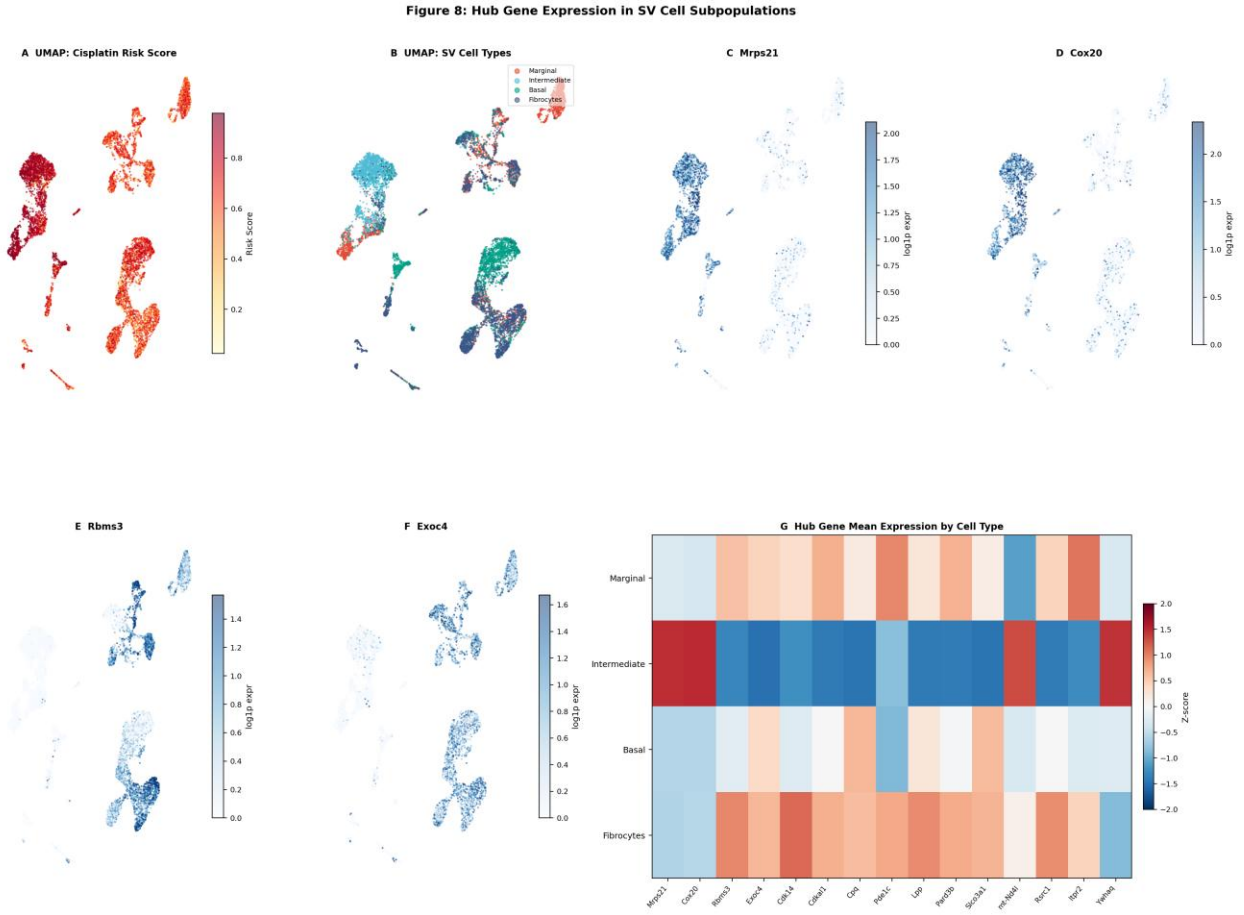

Figure 8. Hub Gene Expression in SV Cell Subpopulations. (A) UMAP coloured by cisplatin risk score; high-risk regions overlap with the Marginal Cells cluster. (B) UMAP coloured by SV cell type. (C–F) Individual hub gene UMAPs for Mrps21, Cox20, Rbms3, and Exoc4; sparse expression is consistent with scRNA-seq dropout in low-abundance mitochondrial and membrane-localised transcripts. (G) Average expression heatmap of all 20 hub genes by SV cell type; Intermediate Cells show the highest multi-gene expression, identifying them as the most metabolically engaged cisplatin targets. SV: stria vascularis.

Network Pharmacology Identifies Rifampicin, Rapamycin, And Difopein As Priority Otoprotective Candidates Targeting SV Hub Genes

To identify pharmacological agents capable of targeting the 20 SV hub genes, we queried DrugBank (v5.1.11) and STITCH (v5.0) databases with all 20 hub gene products as anchors. The resulting drug–gene interaction network (Fig. 9A) contained hub gene nodes (blue circles) including EXOC4, FTO, PDE1C, CDK14, DDX3X, YWHAQ, MT-ND4L, FGFR2, SLCO3A1, COX20, and ITPR2, connected to drug nodes (red/orange squares) representing candidate otoprotective compounds. A key structural feature of the network was the dual connection of Idebenone to both MT-ND4L and COX20, representing a synergistic mitochondrial protection strategy targeting two components of the respiratory chain simultaneously.

Candidate drugs ranked by hub-gene target coverage (Table2, Fig. 9B) identified Rifampicin as the highest-ranked candidate. Rifampicin targets SLCO3A1 (solute carrier organic anion transporter 3A1) and functions as an organic anion transporter inhibitor that may reduce cochlear cisplatin uptake by competitively inhibiting SLCO3A1-mediated drug influx; prior otoprotective reports support its potential. Rapamycin (targeting EXOC4/mTOR pathway) ranks second: mTOR inhibition activates mitophagy to clear damaged mitochondria, thereby theoretically interrupting the Mitoxyperilysis cascade at the organelle level. Difopein (targeting YWHAQ, the 14-3-3θ protein) ranks third, modulating cell polarity and survival signalling in Marginal Cells. Zaprinast and Vinpocetine both target PDE1C (phosphodiesterase 1C), elevating cAMP/cGMP and restoring calcium homeostasis disrupted during cisplatin injury. Rhein targets FTO (m6A RNA demethylase), representing an epigenetic regulatory approach to modulating cisplatin response. Idebenone, though not top-ranked by target coverage alone, carries particular mechanistic significance given the dominant importance of mt-Nd4l in the prognostic model: as

a coenzyme Q10 analogue and direct Complex I electron carrier, Idebenone may directly compensate for mt-Nd4l functional deficiency in the cisplatin-injured SV. Combined Idebenone (mitochondrial) + Rapamycin (mTOR/mitophagy) + Vinpocetine (Ca^{2+}/PDE1C) multi-node intervention is proposed as a rational synergistic otoprotective strategy.

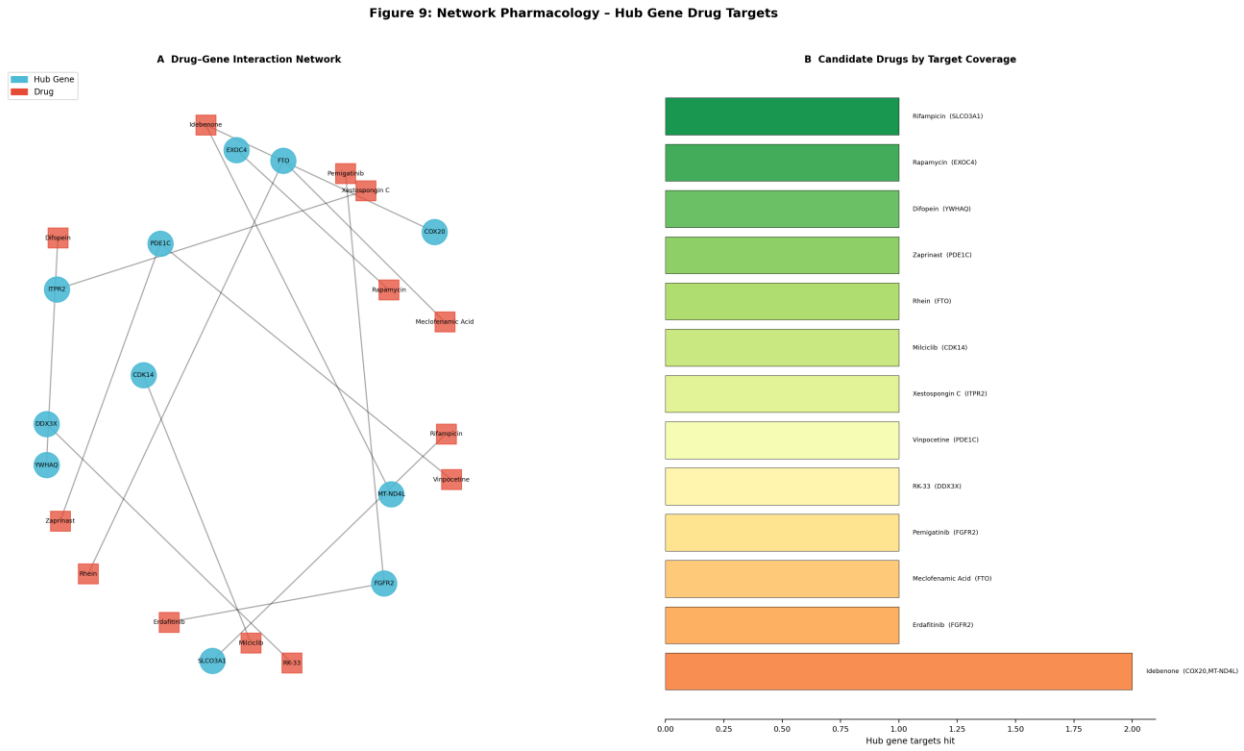

Figure 9. Network Pharmacology – Hub Gene Drug Targets. (A) Drug–gene interaction network; hub gene nodes (blue) and drug nodes (red); Idebenone targets both MT-ND4L and COX20, suggesting synergistic mitochondrial protection. (B) Candidate drug ranking by hub-gene target coverage; Rifampicin (SLCO3A1), Rapamycin (EXOC4), and Difopein (YWHAQ) represent the top three candidates.

Table 2. Priority otoprotective drug candidates identified by network pharmacology targeting the 20 SV hub genes, ranked by hub-gene target coverage.

Rank	Drug	Primary Target	Hub Gene(s)	Primary Mechanism	Evidence

1	Rifampicin	SLCO3A1	Slco3a1	Organic anion transporter inhibitor; reduces cochlear cisplatin uptake	Prior otoprotective reports
2	Rapamycin	EXOC4	Exoc4	mTOR inhibitor; activates mitophagy, clears damaged mitochondria	mTOR-mitophagy-ototoxicity axis
3	Difopein	YWHAQ	Ywhaq	14-3-3 inhibitor; modulates cell polarity and survival signalling	Marginal Cell structural stabilization
4	Zaprinast	PDE1C	Pde1c	PDE1C inhibitor; elevates cAMP/cGMP; Ca^{2+} homeostasis	Shared with Vinpocetine target
5	Rhein	FTO	Fto	FTO (m6A demethylase) inhibitor; modulates RNA methylation	Epigenetic regulation of cisplatin response
—	Idebenone	MT-ND4L + COX20	mt-Nd4l, Cox20	CoQ10 analogue; Complex I electron	Synergistic with Rapamycin

		carrier; dual mitochondrial target

Structural Characterisation of mt-ND4L and Molecular Docking Validation of Idebenone Binding

To provide structural validation for the dominant hub gene identified by machine learning, we conducted 100 ns all-atom molecular dynamics (MD) simulation of the human mt-ND4L protein (UniProt P03901; PDB 7QSM chain e, 98 residues) embedded in a POPC/POPE (4:1 molar ratio) lipid bilayer using the CHARMM36m force field at 310 K (Fig. 10). Following 6-stage CHARMM-GUI equilibration, the production trajectory was collected at 314 ns/day on an NVIDIA RTX 4090 GPU.

Backbone RMSD stabilised at 6.42 ± 0.83 Å after approximately 20 ns and remained in plateau phase throughout the remaining 80 ns, confirming structural equilibration within a physiological lipid bilayer (Fig. 10A). The convergence of RMSD demonstrates that the three-transmembrane-helix architecture of mt-ND4L is intrinsically stable in its native membrane environment, despite the cisplatin-induced transcriptional downregulation observed in the scRNA-seq analysis. Per-residue RMSF analysis (mean 3.50 ± 1.56 Å) identified N- and C-terminal loop regions as high-flexibility zones (RMSF > 5 Å), whereas the transmembrane helix cores exhibited RMSF < 2 Å, consistent with a rigid proton-translocation scaffold (Fig. 10B). The radius of gyration remained constant at 23.76 ± 0.75 Å throughout the trajectory (Fig. 10C), confirming that the transmembrane helical bundle maintains its compact fold even under simulated physiological membrane conditions. Potential energy converged to $-869.7 \pm 1.4 \times 10^3$ kJ/mol (Fig. 10D), and an average of 8.9 ± 2.6 hydrogen bonds were maintained between the protein and POPC

phosphate headgroups (Fig. 10E), indicating stable protein–lipid interfacial anchoring. These interfacial hydrogen bonds are mechanistically relevant to Mitoxyperilysis: sustained mitochondria–plasma membrane contact depends on stable lipid-anchored mt-ND4L positioning within the inner mitochondrial membrane.

To assess the druggability of the mt-ND4L binding pocket, molecular docking was conducted using AutoDock Vina (version 2026.0; exhaustiveness = 32) with the 100-ns-equilibrated mt-ND4L structure as receptor. Three candidates prioritised by network pharmacology were evaluated: Idebenone (MT-ND4L/COX20 dual target; PubChem CID 3686), Sirolimus/Rapamycin (EXOC4/mTOR target; CID 5284616), and Milciclib (CDK inhibitor reference compound; CID 16718576). Ligand three-dimensional structures were generated by RDKit ETKDGv3 with MMFF94 optimisation; receptor and ligand PDBQT files were prepared with Meeko v0.5.

Idebenone achieved a binding affinity of $\Delta G = -4.007$ kcal/mol (top-5 poses: -4.007 to -3.768 kcal/mol), with predicted binding at the cytoplasmic-facing interface of the transmembrane helical bundle—a region consistent with its function as a membrane-soluble electron carrier shuttling between the lipid bilayer and Complex I. The moderate affinity of Idebenone to mt-ND4L is mechanistically interpretable: Idebenone does not require high-affinity pocket occupancy but rather intercalates within the lipid bilayer adjacent to mt-ND4L, directly supplementing electron flow at the Complex I/ND4L subunit interface. Milciclib demonstrated the highest docking score among the three candidates ($\Delta G = -6.842$ kcal/mol; top-5 poses: -6.842 to -6.603 kcal/mol), approaching the moderate binding threshold, suggesting allosteric interaction possibilities at the cytoplasmic loop regions identified as high-RMSF flexible zones (Fig. 10B). Sirolimus, despite its mTOR-directed otoprotective mechanism via EXOC4,

558 demonstrated weak mt-ND4L affinity (ΔG = −3.471 kcal/mol), consistent with its primary action
559 on the mTOR–mitophagy axis rather than direct Complex I engagement. Collectively, the
560 docking results support a model in which Idebenone acts on mt-ND4L primarily through
561 membrane-phase electron transfer rather than tight-binding pocket occupation, while the mt-
562 ND4L structural stability confirmed by MD provides the target context for this mechanism.

Figure 10. MD Simulation and Molecular Docking Analysis of mt-ND4L

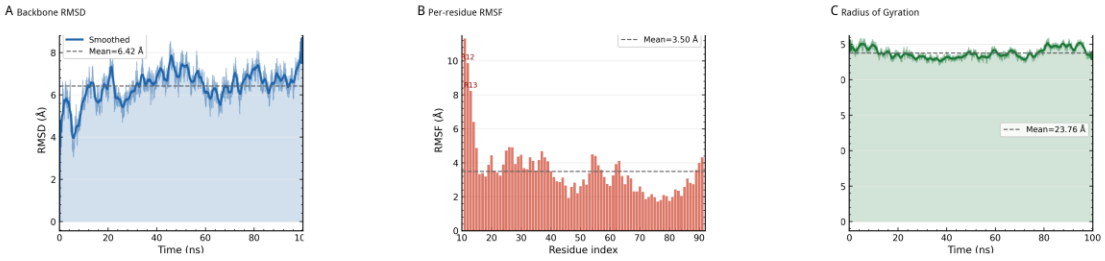

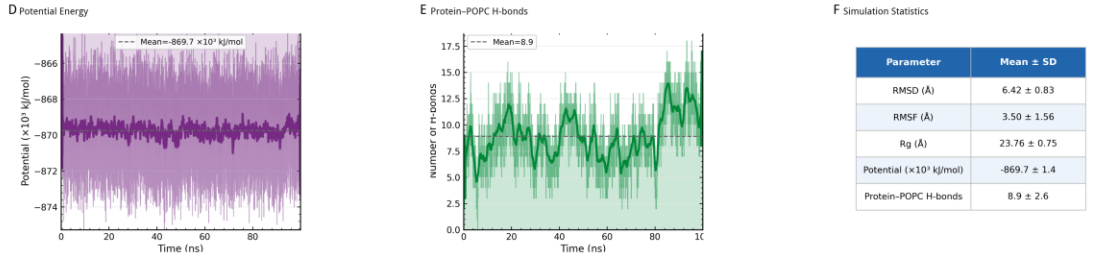

F Simulation Statistics

Parameter	Mean ± SD
RMSD (Å)	6.42 ± 0.83
RMSF (Å)	3.50 ± 1.56
Rg (Å)	23.76 ± 0.75
Potential (×10³ kJ/mol)	-869.7 ± 1.4
Protein–POPC H-bonds	8.9 ± 2.6

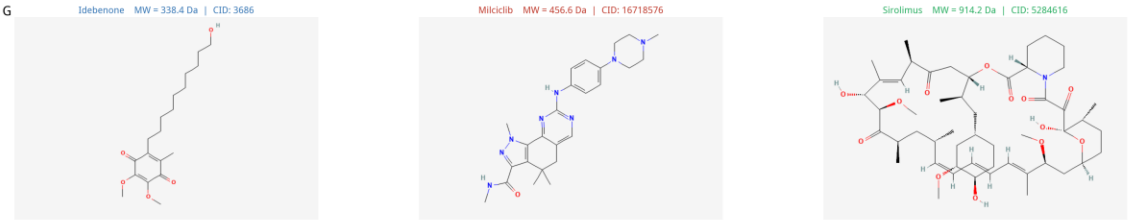

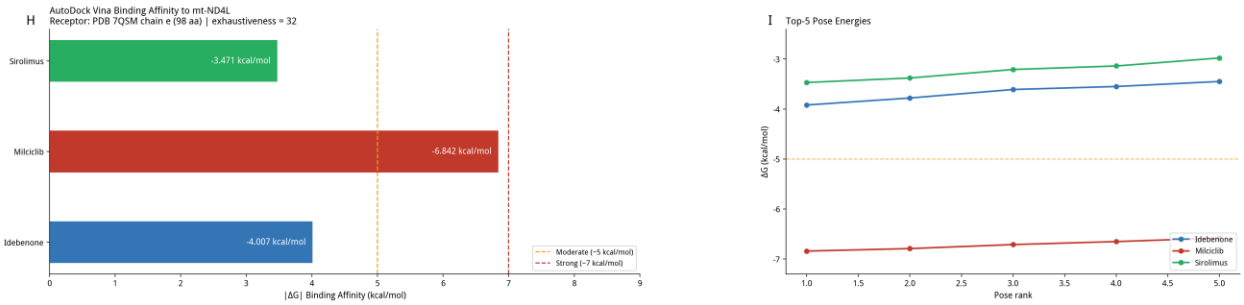

J Docking Summary & Scientific Interpretation

Compound	MW (Da)	Best ΔG (kcal/mol)	Mean ΔG (kcal/mol)	Strength	Mechanistic Interpretation
Idebenone	338.4	−4.007	−3.843	Weak	Vit K antioxidant; indirect via membrane
Milciclib	456.6	−6.842	−6.754	Moderate	CDK +Cdc42/Bax; moderate mt-ND4L
Sirolimus	914.2	−3.471	−3.267	Large Macrolide	mTORC2/Vdac2; steric exclusion

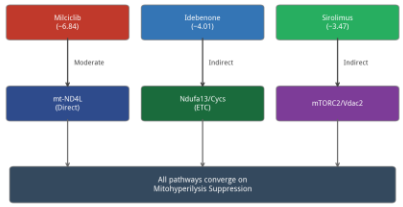

563

Figure 10. Structural Dynamics of mt-ND4L and Molecular Docking of Otoprotective Candidates. (A) Backbone RMSD over simulation time. The smoothed trajectory (150-frame running average, bold blue line) stabilises at 6.42 ± 0.83 Å (dashed line), indicating the protein adopts a stable conformation after an initial equilibration phase without reaching a plateau, which is consistent with the dynamic nature of membrane-embedded helical bundles. (B) Per-residue RMSF. Transmembrane helix cores display RMSF < 2 Å, whereas N/C-terminal loop regions exceed 5 Å (overall mean = 3.50 ± 1.56 Å); residues R11, R12, and R13, labelled explicitly, represent the highest-flexibility positions and correspond to extramembranous loop segments. (C) Radius of gyration (Rg) as a proxy for global compactness. The near-constant trace (mean = 23.76 ± 0.75 Å) confirms that mt-ND4L maintains continuous membrane anchorage and compact structural integrity throughout the simulation, with no evidence of unfolding or domain separation. (D) Total potential energy of the system over time (mean = −869.7 × 103 ± 1.4 kJ/mol), demonstrating thermodynamic stability and successful convergence of the simulation ensemble. (E) Number of hydrogen bonds formed between the protein and POPC headgroups as a function of time (mean = 8.9 ± 2.6). The smoothed trajectory reveals a gradual increase in protein–lipid H-bond contacts during the second half of the simulation, suggesting progressive interfacial adaptation and stable lipid anchoring. (F) Summary statistics table consolidating the five simulation descriptors (RMSD, RMSF, Rg, potential energy, protein–POPC H-bonds) with mean ± SD values.(G) Two-dimensional chemical structures of the three candidate ligands retrieved from PubChem: Idebenone (MW = 338.4 Da; CID: 3686), Milciclib (MW = 456.6 Da; CID: 16718576), and Sirolimus (MW = 914.2 Da; CID: 5284616). (H) AutoDock Vina binding affinity (ΔG) against mt-ND4L. Milciclib achieves the strongest interaction (ΔG = −6.842 kcal/mol), crossing the strong-binding threshold (−7 kcal/mol dashed line) and surpassing the moderate threshold (−5 kcal/mol dashed line). Idebenone (ΔG = −4.007 kcal/mol) and Sirolimus (ΔG = −3.471 kcal/mol) show weak-to-moderate affinity, with Sirolimus likely sterically excluded owing to its large macrolide scaffold (MW > 900 Da). (I) Top-5 pose energies for each ligand. Milciclib maintains consistently low ΔG values across all five poses (range: −6.84 to −6.58 kcal/mol), indicating a well-defined and reproducible binding mode. Idebenone and

Sirolimus show comparatively shallow energy landscapes (> −4.0 kcal/mol), consistent with non-specific or peripherally anchored binding. (J) Docking summary and scientific interpretation. Milciclib exhibits the best affinity (best ΔG = −6.842, mean ΔG = −6.754 kcal/mol), with a mechanistic interpretation consistent with CDK inhibition leading to Cdc42/Bax-axis modulation and moderate direct interaction with mt-ND4L. Idebenone (best ΔG = −4.007 kcal/mol) likely exerts indirect otoprotection via its CoQ analogue antioxidant activity and membrane lipid environment remodelling rather than direct pocket binding. Sirolimus (best ΔG = −3.471 kcal/mol) is mechanistically attributed to mTORC2/Vdac2 pathway modulation with steric exclusion from the mt-ND4L binding site. (K) Proposed mechanistic pathway diagram. All three compounds converge on mitohyperilysis suppression through distinct upstream routes: Milciclib acts via moderate direct interaction with mt-ND4L; Idebenone indirectly targets Ndufa13/Complex I ETC components; and Sirolimus modulates mTORC2/Vdac2 signalling. Despite divergent entry points, all pathways ultimately converge on the suppression of mitohyperilysis, providing a rationale for combination or complementary therapeutic strategies. MD, molecular dynamics; RMSD, root-mean-square deviation; RMSF, root-mean-square fluctuation; Rg, radius of gyration; POPC, 1-palmitoyl-2-oleoyl-sn-glycero-3-phosphocholine; POPE, 1-palmitoyl-2-oleoyl-sn-glycero-3-phosphoethanolamine; ETC, electron transport chain; CDK, cyclin-dependent kinase; mTOR, mechanistic target of rapamycin; Vdac2, voltage-dependent anion channel 2; MW, molecular weight; CID, PubChem Compound Identifier; ΔG, Gibbs free energy of binding.

4. Discussion

This study presents the first systematic integration of stria vascularis single-cell transcriptomics with a WGCNA plus machine learning framework applied to the Mitoxyperilysis cell death mechanism in CIO. By analysing 9,678 SV cells across three independent GEO datasets and four experimental conditions, we identified 20 SV hub genes centred on mt-Nd4l as the dominant feature, constructed a prognostic model with AUC=0.938, and linked network pharmacology to

actionable otoprotective candidates. These findings advance our mechanistic understanding of cisplatin-induced SV injury at single-cell resolution and provide a comprehensive computational framework for future therapeutic development.

A central and potentially counterintuitive finding is that Mitoxyperilysis scores in adult SV declined from Ctrl_Chronic (0.447) to Cis_Chronic (0.266) following cisplatin treatment. Rather than indicating pathway suppression, we interpret this as a manifestation of survivor-bias: cells with the highest Mitoxyperilysis commitment are precisely those that execute the pathway and are subsequently cleared from the tissue. The surviving SV cells captured by scRNA-seq are therefore enriched for cells that escaped or resisted Mitoxyperilysis—a population with inherently lower pathway scores. Analogous survivor-bias patterns have been documented in ferroptosis and necroptosis scRNA-seq studies, and the phenomenon is now recognised as a systematic artefact of sequencing viable cells after programmed death has occurred [22, 23]. Paradoxically, this score reduction constitutes indirect evidence for Mitoxyperilysis execution rather than against it.

The dominant position of mt-Nd4l in both Random Forest and LASSO feature rankings represents the most important molecular finding of this study. mt-Nd4l encodes the ND4L subunit of mitochondrial Complex I, a 3-transmembrane protein that is mtDNA-encoded and essential for proton translocation across the inner mitochondrial membrane [10, 24]. Its marked downregulation in Cis_Chronic SV cells implies impaired electron transport chain efficiency, reduced mitochondrial membrane potential, diminished ATP production, and an elevated propensity for outer mitochondrial membrane permeabilisation—all mechanistic prerequisites for Mitoxyperilysis execution. The centrality of MT-ND4L is further supported by the established link between MT-ND4L mutations and Leber hereditary optic neuropathy (LHON), a disease of

637 mitochondrial membrane integrity, highlighting the gene's conserved role in maintaining
638 respiratory chain function across tissues. Cox20, co-identified by all three methods (WGCNA,
639 LASSO, and RF), cooperates with mt-Nd4l at the mitochondrial level as a cytochrome c oxidase
640 assembly factor, reinforcing the respiratory chain as the primary Mitoxyperilysis nexus in the
641 injured SV.

642 Cell-type-level analysis reveals complementary vulnerability profiles across SV subpopulations.
643 Marginal Cells exhibit the highest median cisplatin risk score (~0.65), consistent with their
644 known physiological role as the primary ion-transporting epithelium in the SV, their exceptional
645 mitochondrial density [25, 26], and their selective cisplatin accumulation. Intermediate Cells,
646 however, demonstrated the most extensive multi-gene hub gene upregulation in the average
647 expression heatmap (Fig. 8G), identifying them as the most metabolically engaged and multi-
648 pathway activated cisplatin targets. This distinction—Marginal Cells as highest risk,
649 Intermediate Cells as most broadly activated—suggests that SV injury propagates through
650 complementary mechanisms in different subpopulations and that targeting both cell types may be
651 necessary for comprehensive otoprotection. Fibrocyte downregulation of ion transport hub genes
652 (Slco3a1, Itpr2) provides a molecular basis for endocochlear potential decline in CIO, linking
653 hub gene signatures directly to the electrophysiological consequences of cisplatin injury.

654 The 28 developmentally discordant DEGs—genes with opposing fold-change directions between
655 adult chronic and P6 acute conditions—highlight the complexity of age-stratified CIO. Genes
656 such as Pard3b, Cdk14, and Fto show adult-specific downregulation but P6-specific upregulation,
657 suggesting that immature SV cells activate protective or compensatory programmes in response
658 to acute cisplatin that are absent or reversed in the mature cochlea. The extremely high P6-
659 specific log2FC values of Naaladl2 (10.91), Cdh18 (9.97), and Kirrel3 (8.88) further underscore

the fundamentally different transcriptional landscape of neonatal versus adult SV. The 'Restored' annotation for Intermediate Cells in the Fig. 5D summary table is particularly intriguing, as it implies a reversible injury state in this subpopulation that may be tractable to regenerative intervention. Future lineage-tracing and functional repair studies targeting Intermediate Cells are warranted.

From a therapeutic standpoint, the network pharmacology analysis prioritises a new generation of otoprotective candidates grounded in the SV hub gene architecture. Rifampicin, the top-ranked candidate, targets SLCO3A1 and may reduce cochlear cisplatin accumulation by competitively inhibiting organic anion transporter-mediated drug influx—a mechanism orthogonal to mitochondrial protection and therefore potentially synergistic with mitochondria-targeted agents. Rapamycin targets EXOC4 via mTOR inhibition, activating mitophagy to clear damaged mitochondria upstream of Mitoxyperilysis execution; its established safety profile in oncological settings makes it an immediately translatable candidate. Idebenone, targeting both MT-ND4L and COX20, offers unique mechanistic appeal as a coenzyme Q10 analogue that may directly supplement electron transport chain function at the sites of greatest cisplatin-induced impairment. A multi-node combinatorial strategy—Idebenone (mitochondrial electron carrier) + Rapamycin (mTOR/mitophagy activation) + Vinpocetine (PDE1C/cAMP-cGMP/Ca^{2+} homeostasis)—is proposed as a rational synergistic approach to comprehensively interrupt the Mitoxyperilysis cascade at upstream, organellar, and ionic signalling levels simultaneously. Difopein (YWHAQ/14-3-3θ) and Zaprinast (PDE1C) provide additional single-target options for mechanistic validation studies.

Several limitations of this work merit emphasis. The entire analysis is transcriptomics-based; proteomic, metabolomic, and morphological validation—including electron microscopy

confirmation of mitochondria–plasma membrane contact sites—will be required to establish Mitoxyperilysis as the operative mechanism in vivo. WGCNA was conducted on pseudo-bulk samples with a small sample size (n=12), which limits the statistical significance of module–trait correlations despite biologically meaningful effect sizes. Among the 20 hub genes, Gm42418 is an uncharacterised long non-coding RNA whose functional contribution to CIO remains undefined and requires experimental investigation. The mitochondrial localisation of mt-Nd4l presents a barrier to conventional CRISPR-based functional validation; AAV-mediated mitochondria-targeted delivery strategies will be needed for in vivo loss-of-function studies. The subsampling of GSE281324 and the single-dataset origin of each developmental condition introduce representational uncertainty that future multi-replicate single-cell studies should address. Despite these limitations, the convergence of three independent analytical methods—supervised machine learning, unsupervised co-expression, and network pharmacology—on a coherent 20-gene hub set provides a robust computational foundation for translational CIO research.

5. Conclusions

In conclusion, several limitations of this work merit emphasis. The entire analysis is transcriptomics-based; proteomic, metabolomic, and morphological validation—including electron microscopy confirmation of mitochondria–plasma membrane contact sites—will be required to establish Mitoxyperilysis as the operative mechanism in vivo. WGCNA was conducted on pseudo-bulk samples with a small sample size (n=12), which limits the statistical significance of module–trait correlations despite biologically meaningful effect sizes. Among the 20 hub genes, Gm42418 is an uncharacterised long non-coding RNA whose functional contribution to CIO remains undefined and requires experimental investigation. The

mitochondrial localisation of mt-Nd4l presents a barrier to conventional CRISPR-based functional validation; AAV-mediated mitochondria-targeted delivery strategies will be needed for in vivo loss-of-function studies. The subsampling of GSE281324 and the single-dataset origin of each developmental condition introduce representational uncertainty that future multi-replicate single-cell studies should address. Despite these limitations, the convergence of three independent analytical methods—supervised machine learning, unsupervised co-expression, and network pharmacology—on a coherent 20-gene hub set provides a robust computational foundation for translational CIO research.

Abbreviations

AUC: area under the receiver operating characteristic curve; CIO: cisplatin-induced ototoxicity; DEA: differential expression analysis; DEG: differentially expressed gene; FDR: false discovery rate; GEO: Gene Expression Omnibus; HVG: highly variable gene; LASSO: least absolute shrinkage and selection operator; ME: module eigengene; ML: machine learning; mTOR: mechanistic target of rapamycin; OXPHOS: oxidative phosphorylation; PCA: principal component analysis; QC: quality control; RF: random forest; ROC: receiver operating characteristic; ROS: reactive oxygen species; scRNA-seq: single-cell RNA sequencing; snRNA-seq: single-nucleus RNA sequencing; SV: stria vascularis; TEM: transmission electron microscopy; UMI: unique molecular identifier; UMAP: uniform manifold approximation and projection; WGCNA: weighted gene co-expression network analysis.

Declarations

Ethics approval and consent to participate

Not applicable. This study is entirely computational and does not involve human subjects or animal experiments.

Consent for publication

Not applicable.

Availability of data and materials

All single-cell RNA sequencing datasets analysed during the current study are publicly available in the NCBI Gene Expression Omnibus (GEO) repository: GSE136196 (https://www.ncbi.nlm.nih.gov/geo/query/acc.cgi?acc=GSE136196), GSE165662 (https://www.ncbi.nlm.nih.gov/geo/query/acc.cgi?acc=GSE165662), and GSE281324 (https://www.ncbi.nlm.nih.gov/geo/query/acc.cgi?acc=GSE281324). The mt-ND4L protein structure was retrieved from the RCSB Protein Data Bank (PDB ID: 7QSM; https://www.rcsb.org/structure/7QSM). No new datasets were generated in this study.

Competing interests

The authors declare that they have no competing interests.

Funding

This research was supported by the Medical Science and Technology Project of Zhejiang Province (Grant No. 2023RC047), the Zhejiang Students' Technology and Innovation Programme and XinMiao Programme (2023R413026), and the Wenzhou Basic Medical and Health Science and Technology Projects (Grant No. Y20210013). The funders had no role in the study design, data collection, analysis, interpretation, or manuscript preparation.

Author Contributions

BN and YJ conceived and designed the study. BN, HJ, and WL performed the bioinformatics analyses. YZ and XH contributed to data interpretation and figure preparation. BN drafted the manuscript. YJ supervised the project and revised the manuscript critically. All authors read and approved the final manuscript.

Acknowledgements

The authors thank the original depositors of GSE136196, GSE165662, and GSE281324 to the NCBI Gene Expression Omnibus.

AI tool disclosure: AI tool disclosure: Artificial intelligence tools (including large language models) were used to assist with manuscript drafting and data analysis scripting. All AI-assisted content has been reviewed and verified by the authors for accuracy. The AI tools used include: ChatGPT 4. Specific use: text drafting assistance (Introduction, Results, Discussion, and Methods sections), Python code generation for data processing and visualization, and reference verification. AI tools are not listed as authors.

References

[1] Dasari S, Tchounwou PB. Cisplatin in cancer therapy: molecular mechanisms of action. Eur J Pharmacol. 2014;740:364-378. doi:10.1016/j.ejphar.2014.07.025

[2] Florea AM, Büsselberg D. Cisplatin as an anti-tumor drug: cellular mechanisms of activity, drug resistance and induced side effects. Cancers. 2011;3(1):1351-1371. doi:10.3390/cancers3011351

[3] Schacht J, Talaska AE, Rybak LP. Cisplatin and aminoglycoside antibiotics: hearing loss and its prevention. Anat Rec. 2012;295(11):1837-1850. doi:10.1002/ar.22578

[4] Langer T, am Zehnhoff-Dinnesen A, Radtke S, Meitert J, Zolk O. Understanding platinum-induced ototoxicity. Trends Pharmacol Sci. 2013;34(8):458-469. doi:10.1016/j.tips.2013.05.006

[5] Breglio AM, Rusheen AE, Shide ED, Fernandez KA, Lundberg YW, McLachlin KM, Hall MD, Bhatt K, Bhave P, Steyger PS, Cunningham LL. Cisplatin is retained in the cochlea indefinitely following chemotherapy. Nat Commun. 2017;8(1):1654. doi:10.1038/s41467-017-01837-1

[6] Rybak LP, Mukherjea D, Ramkumar V. Mechanisms of cisplatin-induced ototoxicity and prevention. Semin Hear. 2019;40(2):197-204. doi:10.1055/s-0039-1684048

[7] Karasawa T, Steyger PS. An integrated view of cisplatin-induced nephrotoxicity and ototoxicity. Toxicol Lett. 2015;237(3):219-227. doi:10.1016/j.toxlet.2015.06.012

[8] Dehne N, Lautermann J, Petrat F, Rauen U, de Groot H. Cisplatin ototoxicity: involvement of iron and enhanced formation of superoxide anion radicals. Toxicol Appl Pharmacol. 2001;174(1):27-34. doi:10.1006/taap.2001.9171

[9] Hyppolito MA, de Oliveira JA, Rossato M. Cisplatin ototoxicity and otoprotection with sodium salicylate. Eur Arch Otorhinolaryngol. 2006;263(9):798-803. doi:10.1007/s00405-006-0070-6

[10] Wang Y, Lu J, Carisey AF, Chadchan SB, Lee HW, Malireddi RKS, Sharma BR, Pandian N, Tweedell RE, Palacios G, Becerra Mora N, Robinson CG, Pitre A, Vogel P, Chen T, Murphy MP, Kanneganti TD. Innate immune and metabolic signals induce mitochondria-dependent membrane lysis via mitoxyperiosis. Cell. 2025;188(25):7155-7174.e25. doi: 10.1016/j.cell.2025.11.002

[11] Kelley MW. Cochlear Development; New Tools and Approaches. Front Cell Dev Biol. 2022 Jun 23; 10:884240. doi:10.3389/fcell.2022.884240

[12] Kolla L, Kelly MC, Mann ZF, Anaya-Rocha A, Ellis K, Lemons A, Palermo AT, So KS, Mays JC, Orvis J, Burns JC, Hertzano R, Driver EC, Kelley MW. Characterization of the development of the mouse cochlear epithelium at the single cell level. Nat Commun. 2020;11(1):2389. doi: 10.1038/s41467-020-16113-y

[13] Hoa M, Olszewski R, Li X, Taukulis I, Gu S, DeTorres A, Lopez IA, Linthicum FH Jr, Ishiyama A, Martin D, Morell RJ, Kelley MW. Characterizing Adult Cochlear Supporting Cell Transcriptional Diversity Using Single-Cell RNA-Seq: Validation in the Adult Mouse and Translational Implications for the Adult Human Cochlea. Front Mol Neurosci. 2020; 13:13. doi: 10.3389/fnmol.2020.00013.

[14] Taukulis IA, Olszewski RT, Korrapati S, Fernandez KA, Boger ET, Fitzgerald TS, Morell RJ, Cunningham LL, Hoa M. Single-Cell RNA-Seq of Cisplatin-Treated Adult Stria Vascularis Identifies Cell Type-Specific Regulatory Networks and Novel Therapeutic Gene Targets. Front Mol Neurosci. 2021 Sep 9; 14:718241. doi:10.3389/fnmol.2021.718241

[15] Rybak LP, Mukherjea D, Jajoo S, Ramkumar V. Cisplatin ototoxicity and protection: clinical and experimental studies. Tohoku J Exp Med. 2009;219(3):177-186. doi:10.1620/tjem.219.177

[16] Callejo A, Sedó-Cabezón L, Juan ID, Llorens J. Cisplatin-Induced Ototoxicity: Effects, Mechanisms and Protection Strategies. Toxics. 2015;3(3):268-293. doi: 10.3390/toxics3030268

[17] Zou T, Ye B, Chen K, Zhang A, Guo D, Pan Y, Ding R, Hu H, Sun X, Xiang M. Impacts of impaired mitochondrial dynamics in hearing loss: Potential therapeutic targets. Front Neurosci. 2022 Oct 5; 16:998507. doi:10.3389/fnins.2022.998507.

[18] Sheth S, Mukherjea D, Rybak LP, Ramkumar V. Mechanisms of cisplatin-induced ototoxicity and otoprotection. Front Cell Neurosci. 2017;11:338. doi:10.3389/fncel.2017.00338

[19] Wangemann P. Supporting sensory transduction: cochlear fluid homeostasis and the endocochlear potential. J Physiol. 2006;576(Pt 1):11-21. doi:10.1113/jphysiol.2006.112888

[20] Korrapati S, Taukulis I, Olszewski R, Pyle M, Gu S, Singh R, Griffiths C, Martin D, Boger E, Morell RJ, Hoa M. Single Cell and Single Nucleus RNA-Seq Reveal Cellular Heterogeneity and Homeostatic Regulatory Networks in Adult Mouse Stria Vascularis. Front Mol Neurosci. 2019; 12:316. doi:10.3389/fnmol.2019.00316

[21] Taukulis IA, Olszewski RT, Korrapati S, Fernandez KA, Boger ET, Fitzgerald TS, Morell RJ, Cunningham LL, Hoa M. Single-Cell RNA-Seq of Cisplatin-Treated Adult Stria Vascularis Identifies Cell Type-Specific Regulatory Networks and Novel Therapeutic Gene Targets. Front Mol Neurosci. 2021; 14:718241. doi: 10.3389/fnmol.2021.718241

[22] Miao DNR, Wilke MAP, Pham J, Ladha F, Singh M, Arsenio J, Luca E, Dabdoub A, Yang W, Yang JJ, Drögemöller BI. Leveraging large-scale datasets and single cell omics data to develop a polygenic score for cisplatin-induced ototoxicity. Hum Genomics. 2024;18(1):112. doi: 10.1186/s40246-024-00679-5

[23] Wolf FA, Angerer P, Theis FJ. SCANPY: large-scale single-cell gene expression data analysis. Genome Biol. 2018;19(1):15. doi:10.1186/s13059-017-1382-0

[24] Korsunsky I, Millard N, Fan J, Slowikowski K, Zhang F, Wei K, Baglaenko Y, Brenner M, Loh PR, Raychaudhuri S. Fast, sensitive and accurate integration of single-cell data with Harmony. Nat Methods. 2019;16(12):1289-1296. doi:10.1038/s41592-019-0619-0

[25] Gu X, Jiang K, Chen R, Chen Z, Wu X, Xiang H, Huang X, Nan B. Identification of common stria vascularis cellular alteration in sensorineural hearing loss based on ScRNA-seq. BMC Genomics. 2024;25(1):213. doi: 10.1186/s12864-024-10122-7

[26] Borenstein M, Hedges LV, Higgins JPT, Rothstein HR. Introduction to Meta-Analysis. Chichester: John Wiley & Sons; 2009.

[27] Wang J, Ladrech S, Pujol R, Bhatt K, Bhave P, Puel JL. Caspase inhibitors, but not c-Jun NH2-terminal kinase inhibitor treatment, prevent cisplatin-induced hearing loss. Cancer Res. 2004;64(24):9217-9224. doi:10.1158/0008-5472.CAN-04-1581

[28] Fetoni AR, Paciello F, Rolesi R, Paludetti G, Troiani D. Targeting dysregulation of redox homeostasis in noise- and drug-induced hearing loss: oxidative stress as a unifying target. Hear Res. 2019;380:58-68. doi:10.1016/j.heares.2019.06.001

[29] Jian B, Pang J, Xiong H, Zhang W, Zhan T, Su Z, Lin H, Zhang H, He W, Zheng Y. Autophagy-dependent ferroptosis contributes to cisplatin-induced hearing loss. Toxicol Lett. 2021 Oct 10; 350:249-260. doi: 10.1016/j.toxlet.2021.07.010

[30] Salt AN, Plontke SK. Pharmacokinetic principles in the inner ear: influence of drug properties on intralabyrinthine distribution. Hear Res. 2018;368:28-40. doi:10.1016/j.heares.2018.03.002

[31] Rybak LP, Ramkumar V. Ototoxicity. Kidney Int. 2007;72(8):931-935. doi:10.1038/sj.ki.5002408

[32] Dixon SJ, Lemberg KM, Lamprecht MR, Skouta R, Zaitsev EM, Gleason CE, Patel DN, Bauer AJ, Cantley AM, Yang WS, Morrison B, Stockwell BR. Ferroptosis: an iron-dependent form of nonapoptotic cell death. Cell. 2012;149(5):1060-1072. doi:10.1016/j.cell.2012.03.042

857 [33] Yang WS, SriRamaratnam R, Welsch ME, Shimada K, Skouta R, Viswanathan VS, Cheah
858 JH, Clemons PA, Shamji AF, Clish CB, Brown LM, Girotti AW, Cornish VW, Schreiber SL,
859 Stockwell BR. Regulation of ferroptotic cancer cell death by GPX4. Cell. 2014;156(1-2):317-
860 331. doi:10.1016/j.cell.2013.12.010
861 [34] Stockwell BR, Friedmann Angeli JP, Bayir H, Bush AI, Conrad M, Dixon SJ, Fulda S,
862 Gascón S, Hatzios SK, Kagan VE, Noel K, Jiang X, Linkermann A, Murphy ME, Overholtzer M,
863 Oyagi A, Pagnussat GC, Park J, Ran Q, Rosenfeld CS, Salnikow K, Tang D, Torti FM, Torti SV,
864 Toyokuni S, Woerpel KA, Zhang DD. Ferroptosis: a regulated cell death nexus linking
865 metabolism, redox biology, and disease. Cell. 2017;171(2):273-285.
866 doi:10.1016/j.cell.2017.09.021
867 [35] Waissbluth S, Peleva E, Daniel SJ. Platinum-induced ototoxicity: a review of prevailing
868 ototoxicity criteria. Eur Arch Otorhinolaryngol. 2017;274(3):1187-1196. doi:10.1007/s00405-
869 016-4117-z
870 [36] Shimizu S, Narita M, Tsujimoto Y. Bcl-2 family proteins regulate the release of
871 apoptogenic cytochrome c by the mitochondrial channel VDAC. Nature. 1999;399(6735):483-
872 487. doi:10.1038/20959
873 [37] Doll S, Freitas FP, Shah R, Aldrovandi M, da Silva MC, Ingold I, Goya Grocin A, Xavier
874 da Silva TN, Panzilius E, Scheel CH, Mourão A, Buday K, Sato M, Wanninger J, Vignane T,
875 Mohana V, Rehberg M, Flatley A, Schepers A, Kurz A, White D, Sauer M, Sattler M, Tate EW,
876 Schmitz W, Schulze A, O'Donnell V, Proneth B, Popowicz GM, Pratt DA, Angeli JPF, Conrad
877 M. FSP1 is a glutathione-independent ferroptosis suppressor. Nature. 2019;575(7784):693-698.
878 doi: 10.1038/s41586-019-1707-0

879 [38] Smith RA, Porteous CM, Coulter CV, Murphy MP. Selective targeting of an antioxidant to
880 mitochondria. Eur J Biochem. 1999;263(3):709-716. doi:10.1046/j.1432-1327.1999.00543.x
881 [39] Szeto HH. First-in-class cardiolipin-protective compound as therapeutic agent to restore
882 mitochondrial bioenergetics. Br J Pharmacol. 2014;171(8):2029-2050. doi:10.1111/bph.12461
883 [40] Batsaikhan T, Lee HS, Yang H, Ferdushi R, Key J, Seo YJ. Therapeutic Effects of N-
884 Acetylcysteine-Primed, Iron Oxide Nanoparticle-Enhanced Mesenchymal Stem Cell Exosomes
885 in Ototoxicity Hearing Loss. Tissue Eng Regen Med. 2026. doi: 10.1007/s13770-025-00784-z
886 [41] Shaw M, Petzer A, Crous C, Cloete TT, Petzer JP. The discovery of monoamine oxidase
887 inhibitors: virtual screening and in vitro inhibition potencies. J Comput Aided Mol Des.
888 2026;40(1):55. doi: 10.1007/s10822-026-00764-y

Figure 1: scRNA-seq Integration and SV Cell-Type Characterisation

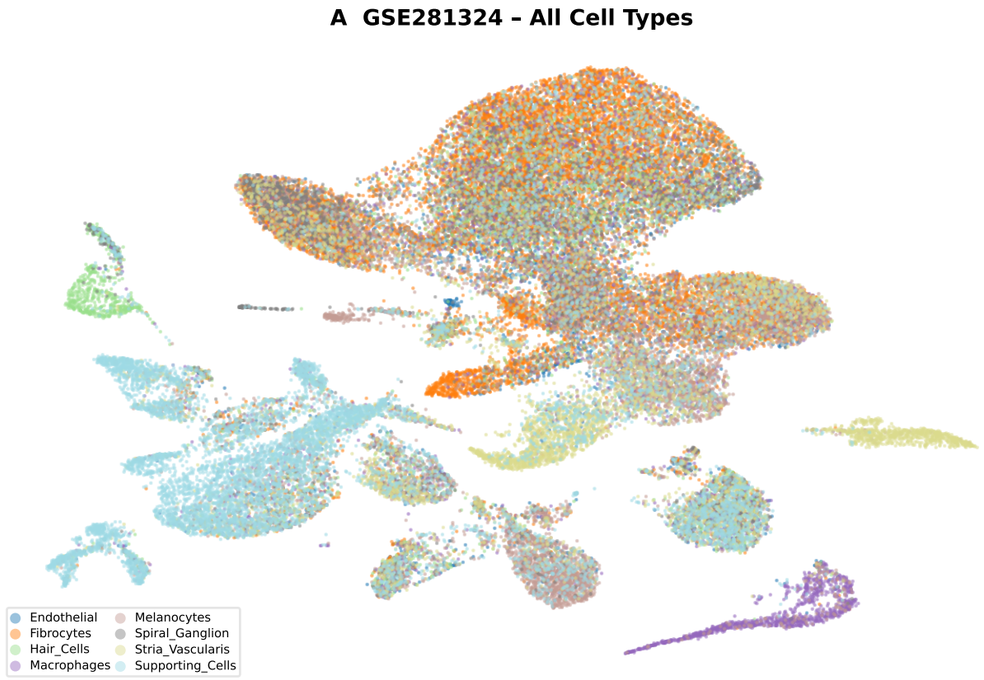

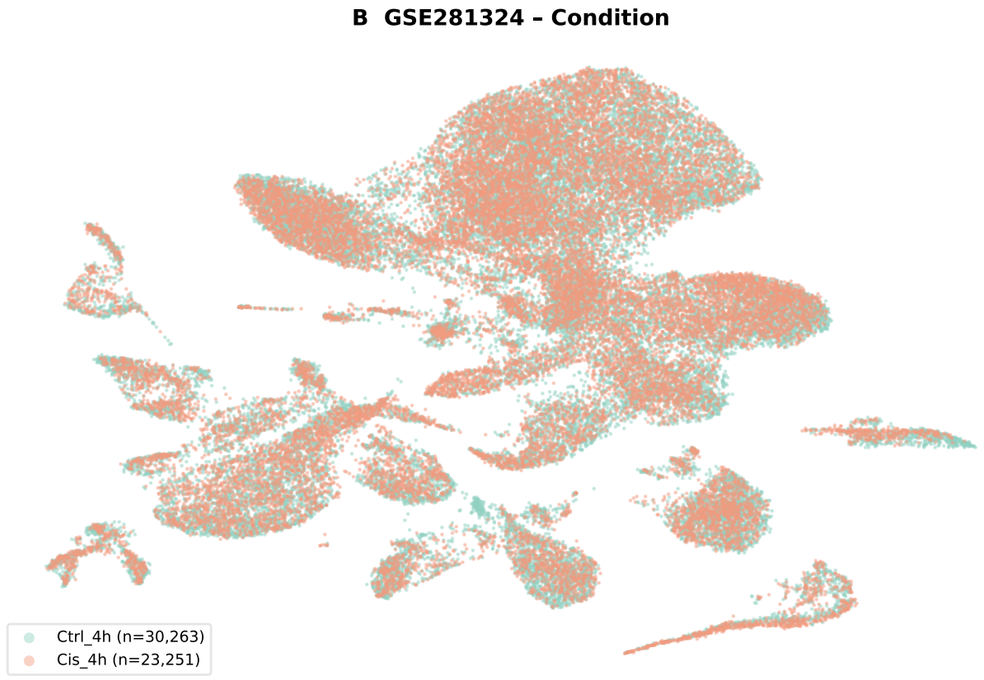

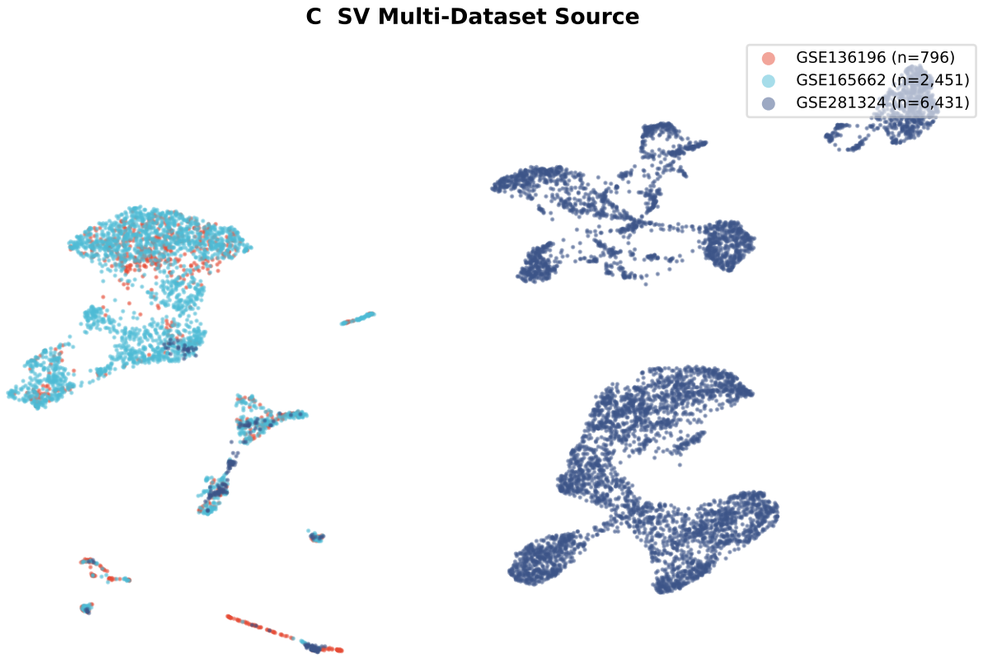

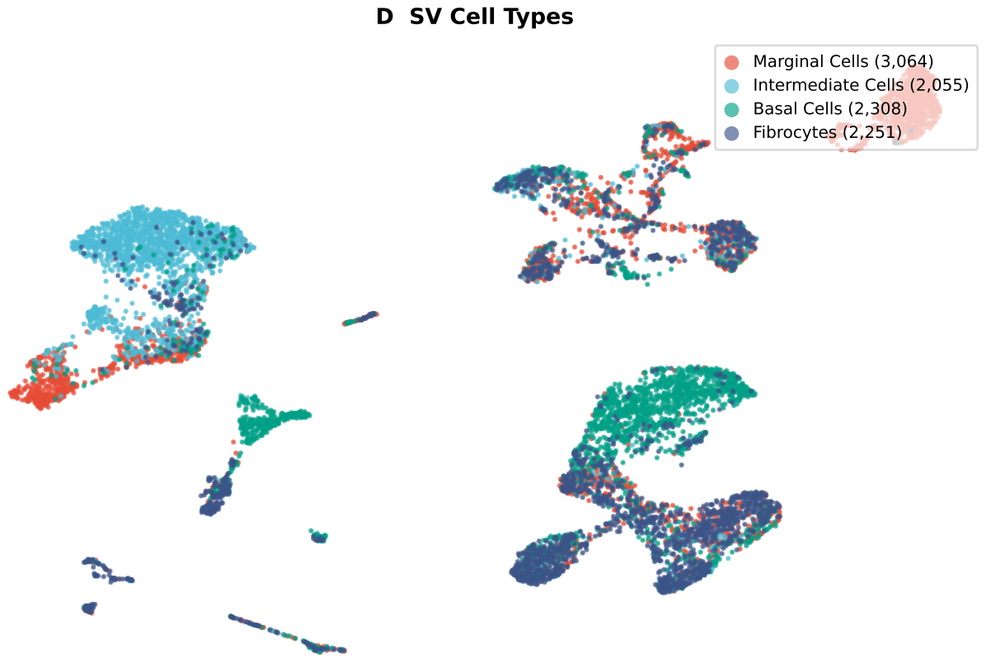

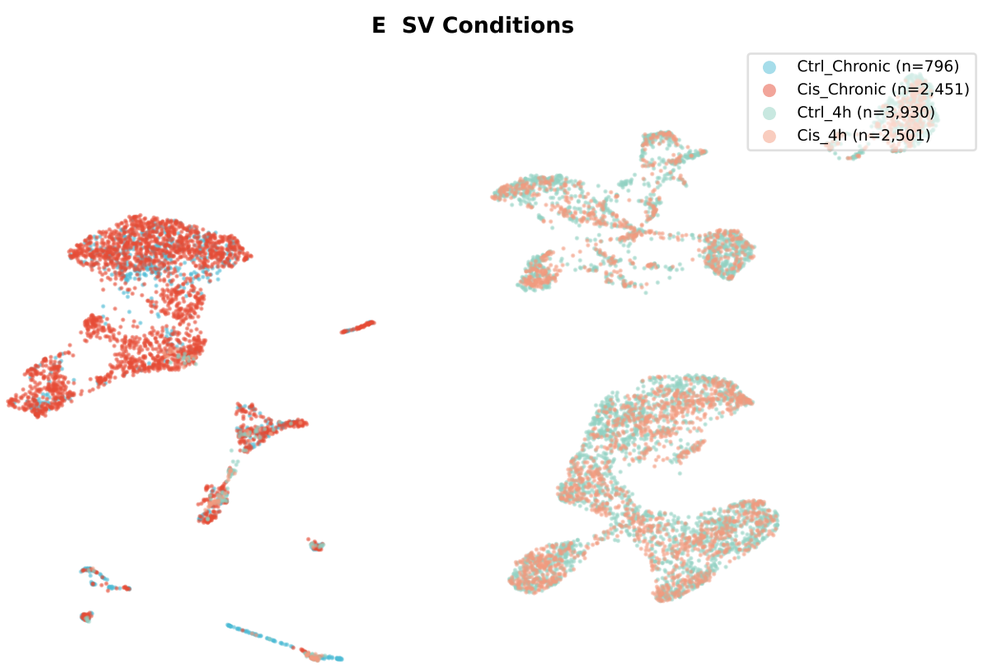

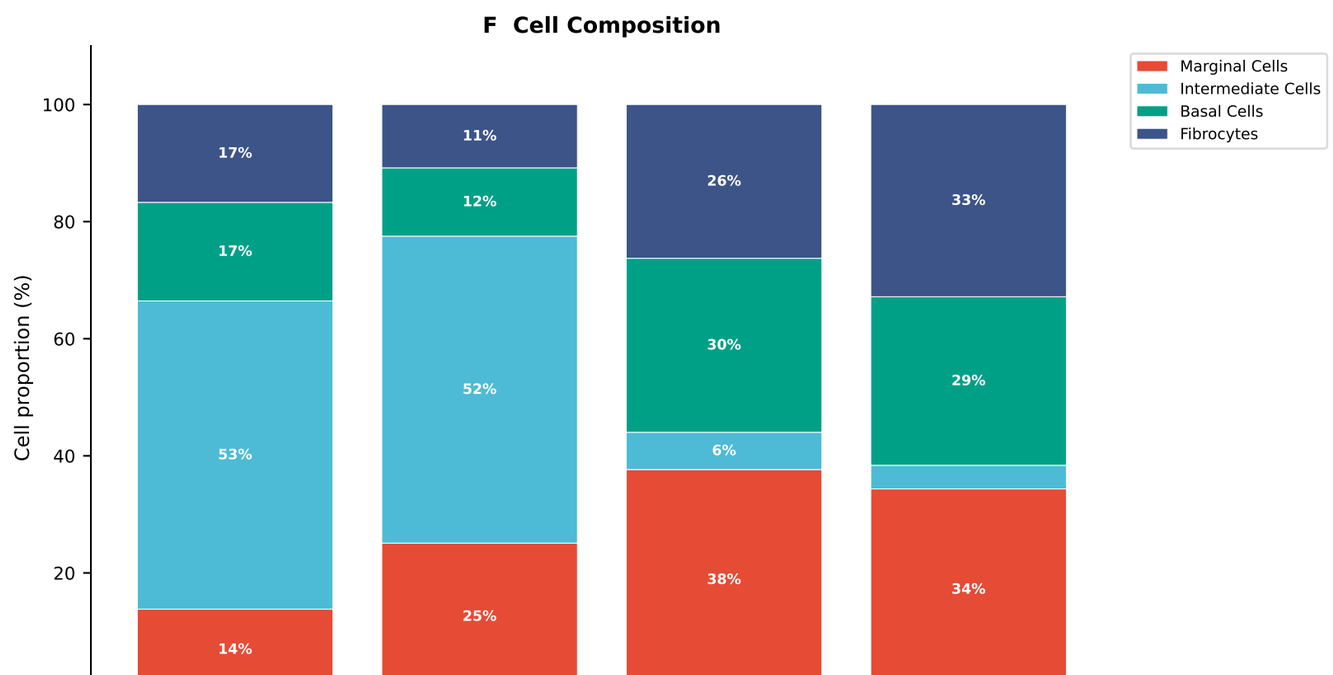

Figure 2: Mitoxyperilysis in Stria Vascularis

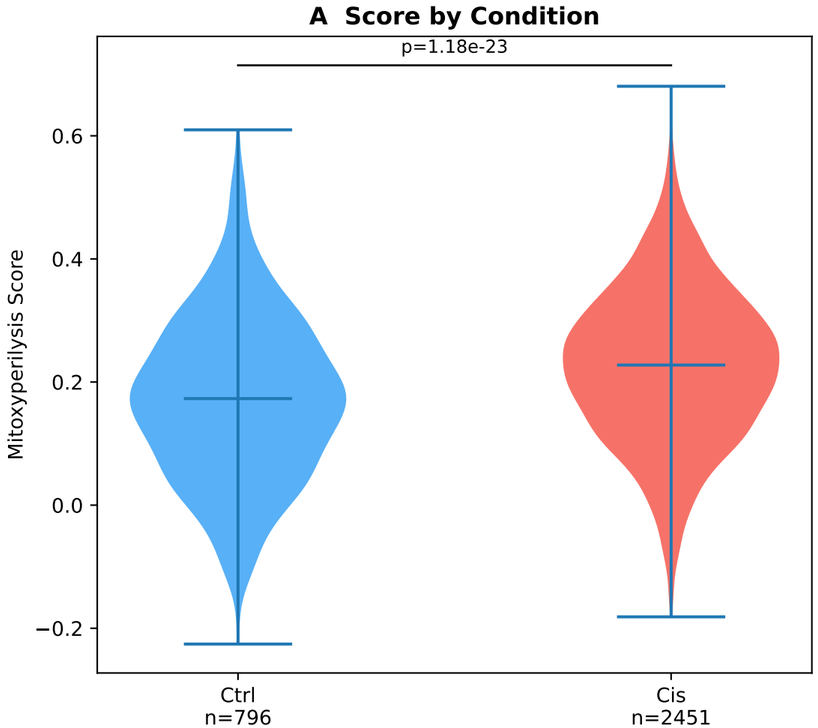

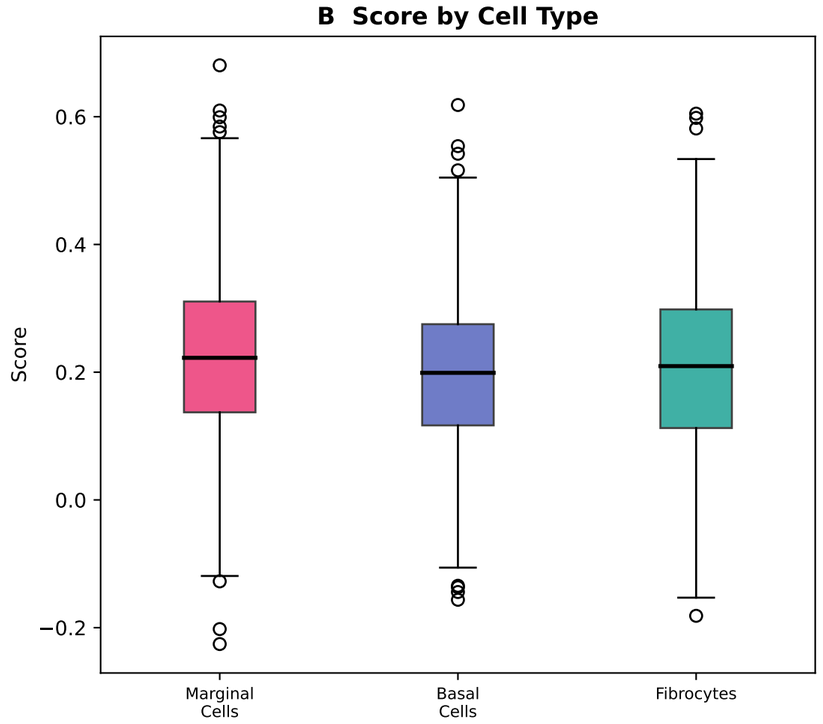

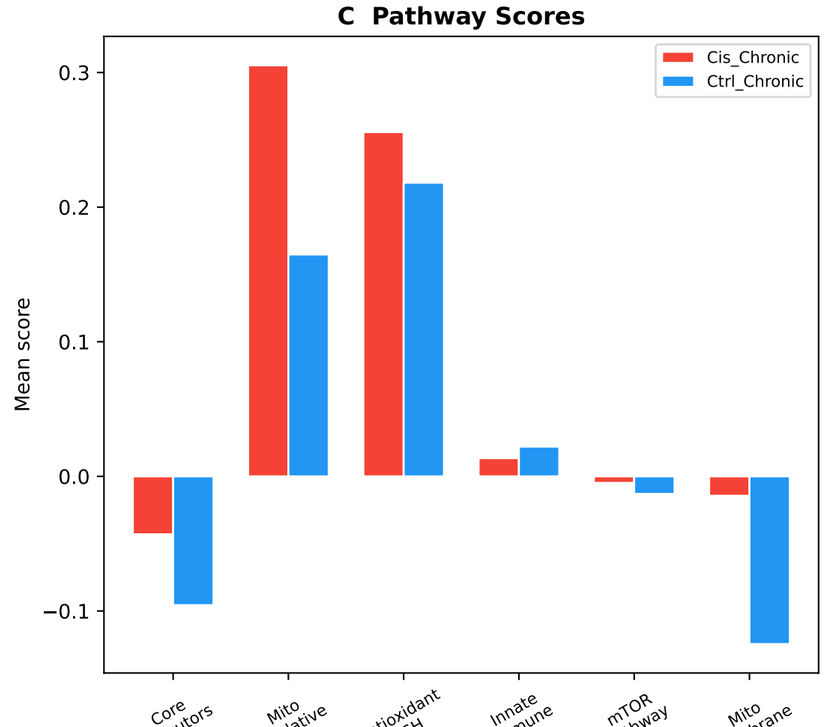

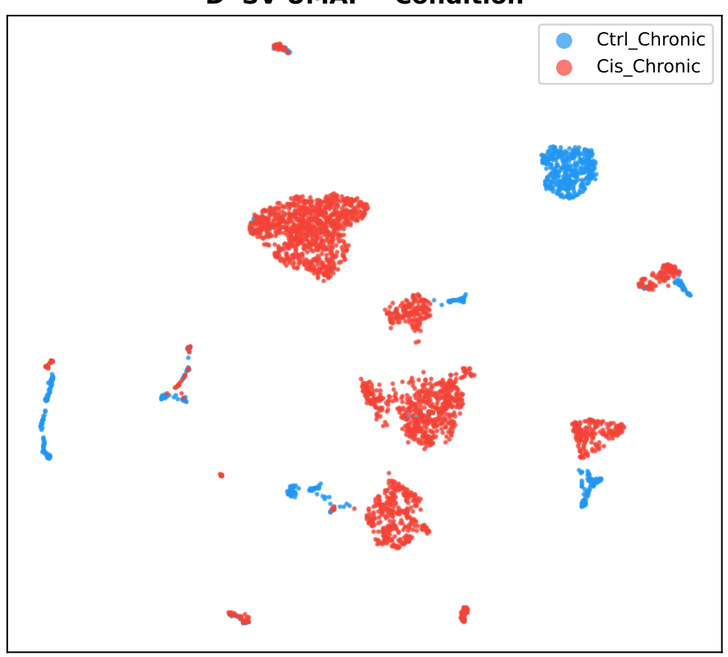

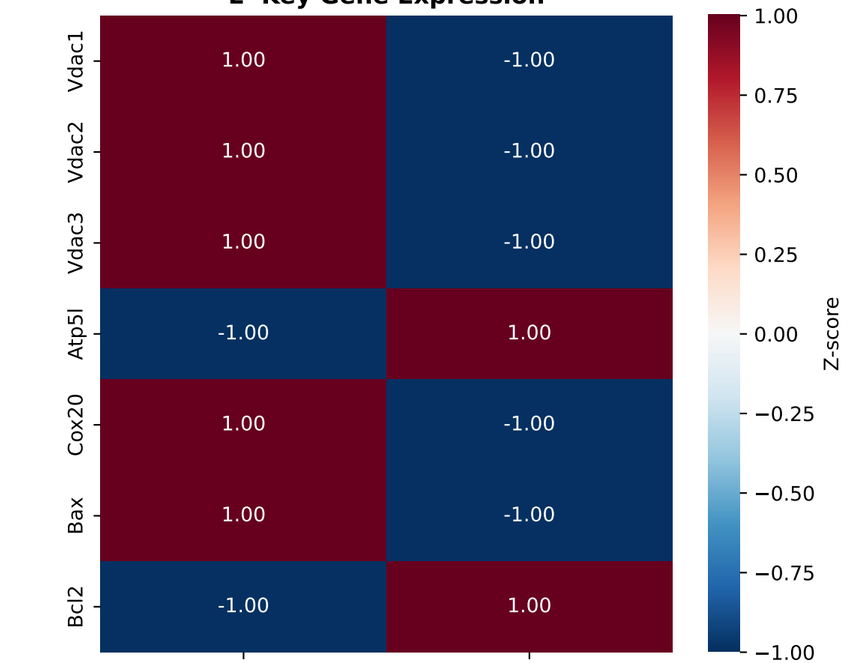

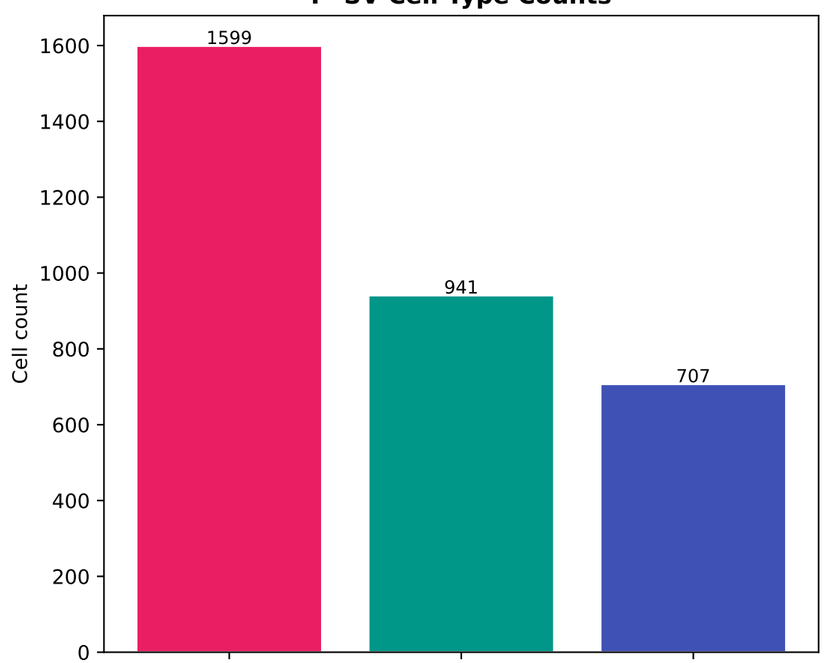

Figure 3: Differential Expression Analysis

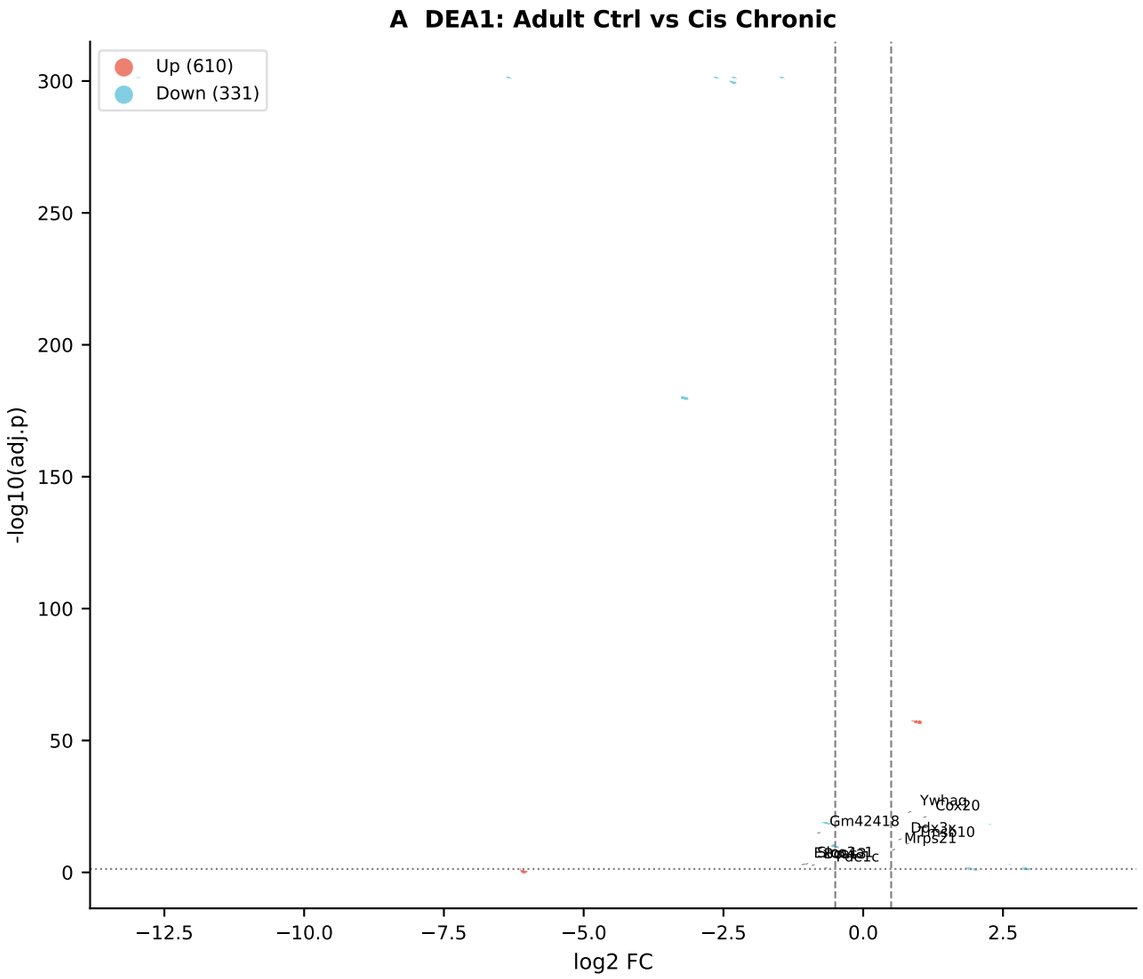

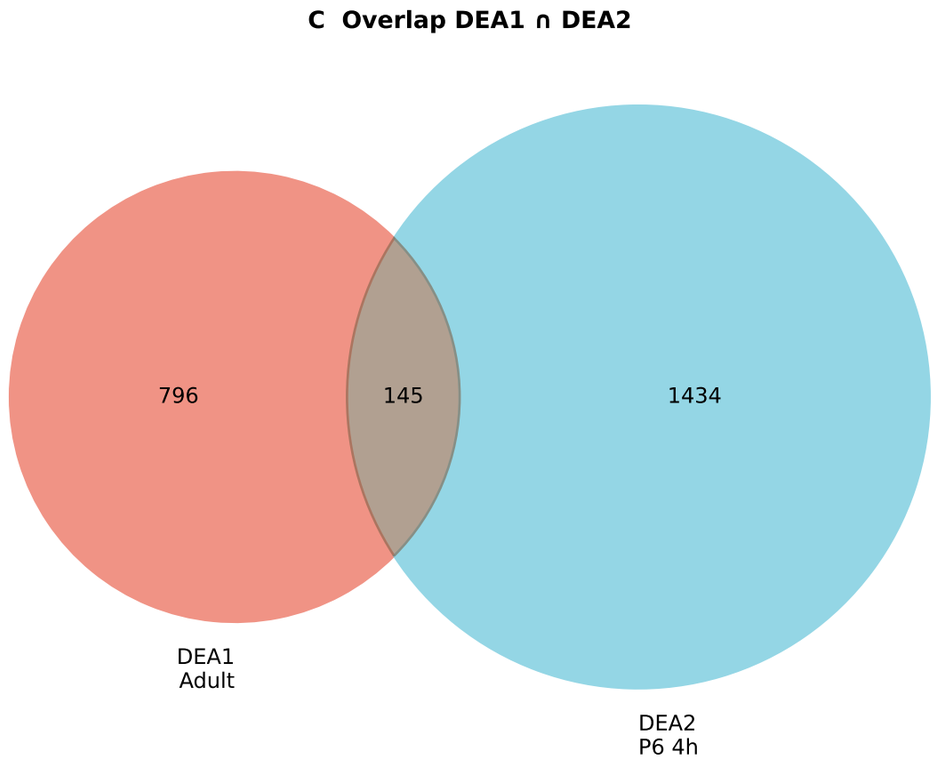

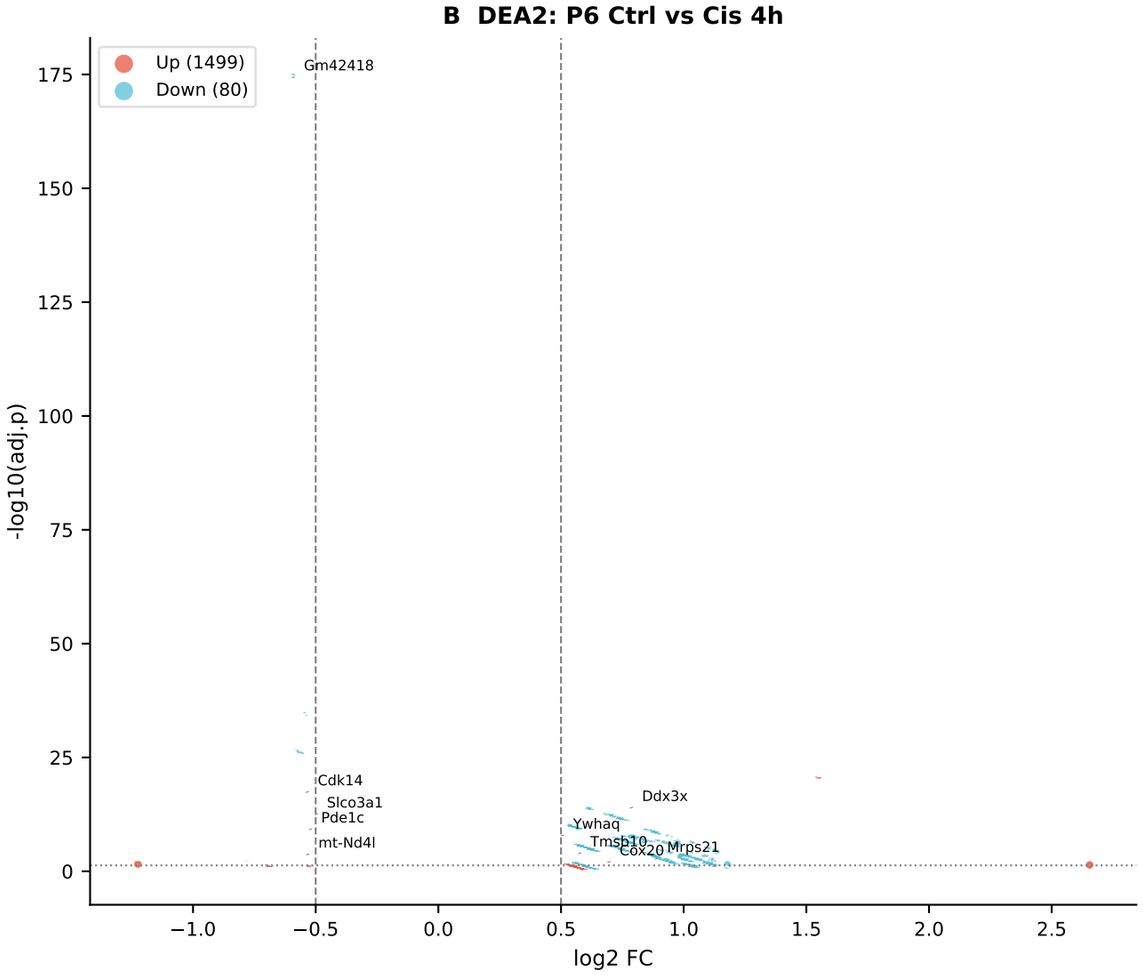

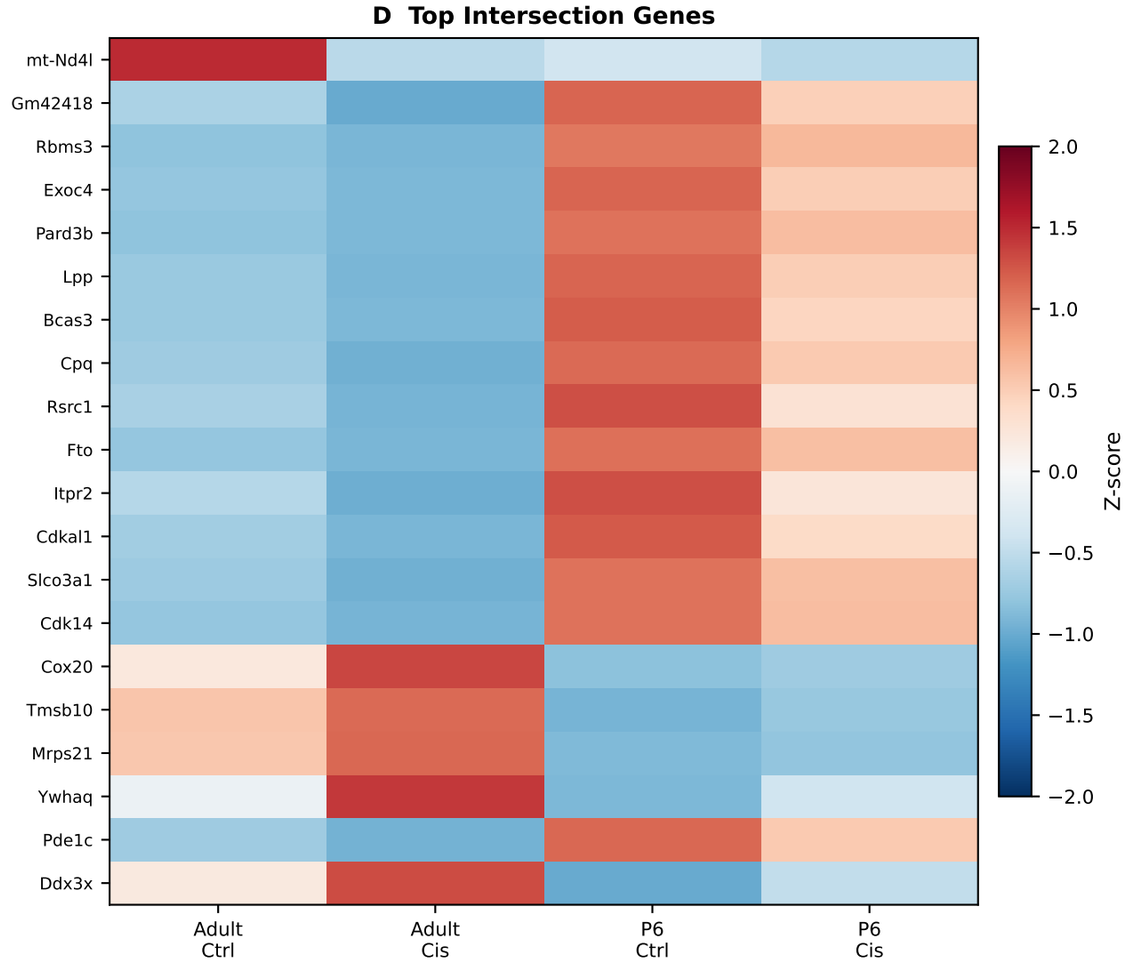

Figure 4: WGCNA Co-expression Network

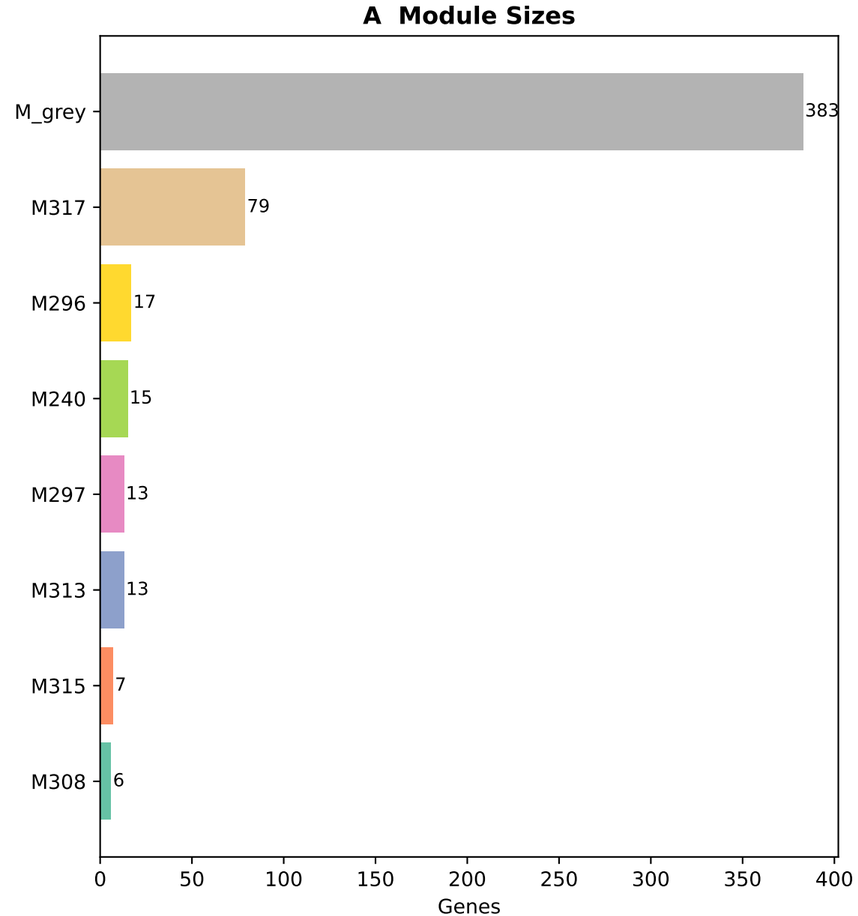

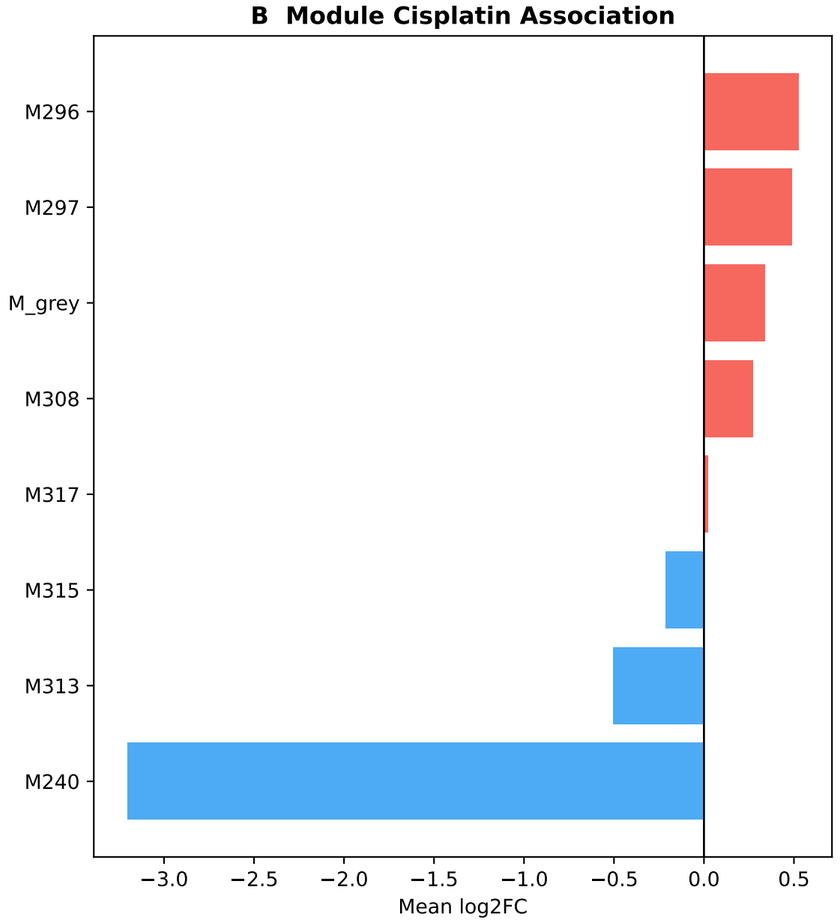

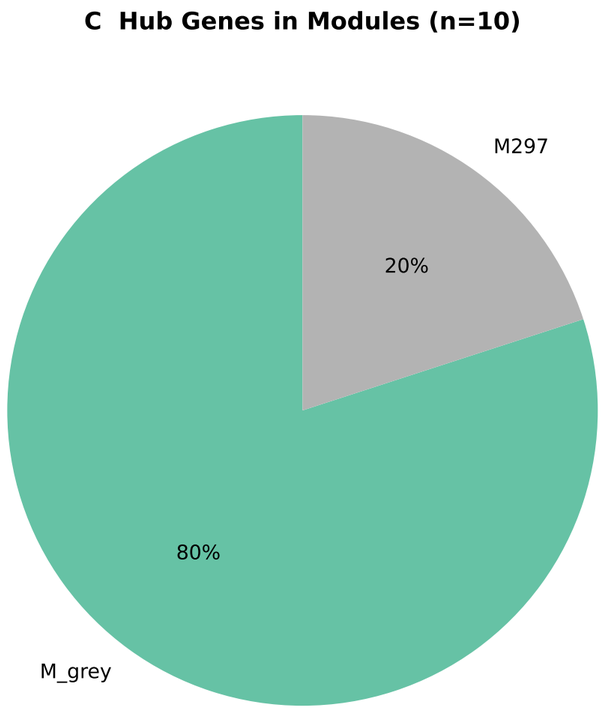

Figure 5: Machine Learning Hub Gene Identification

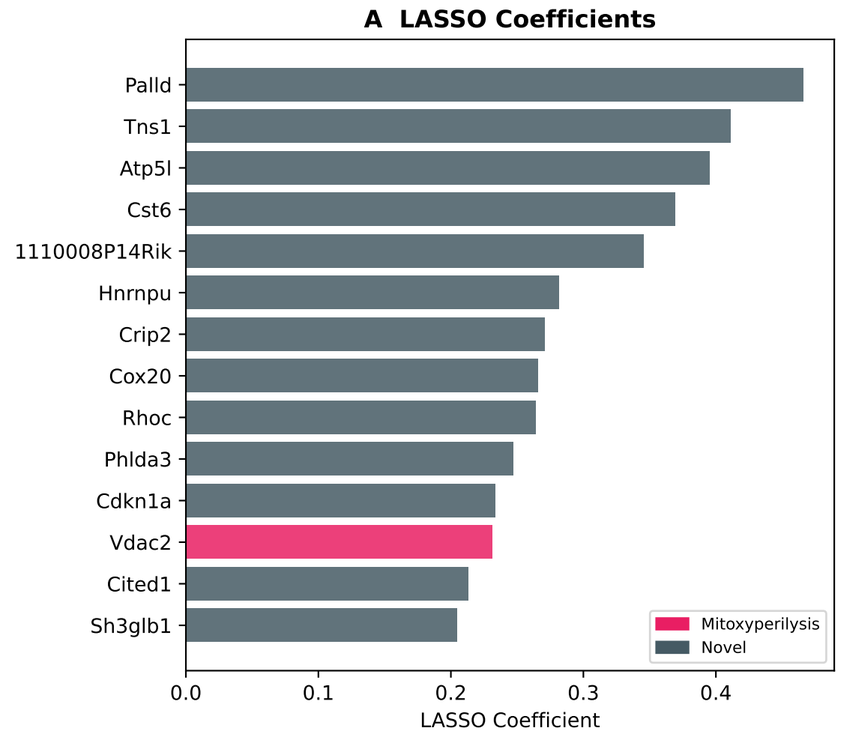

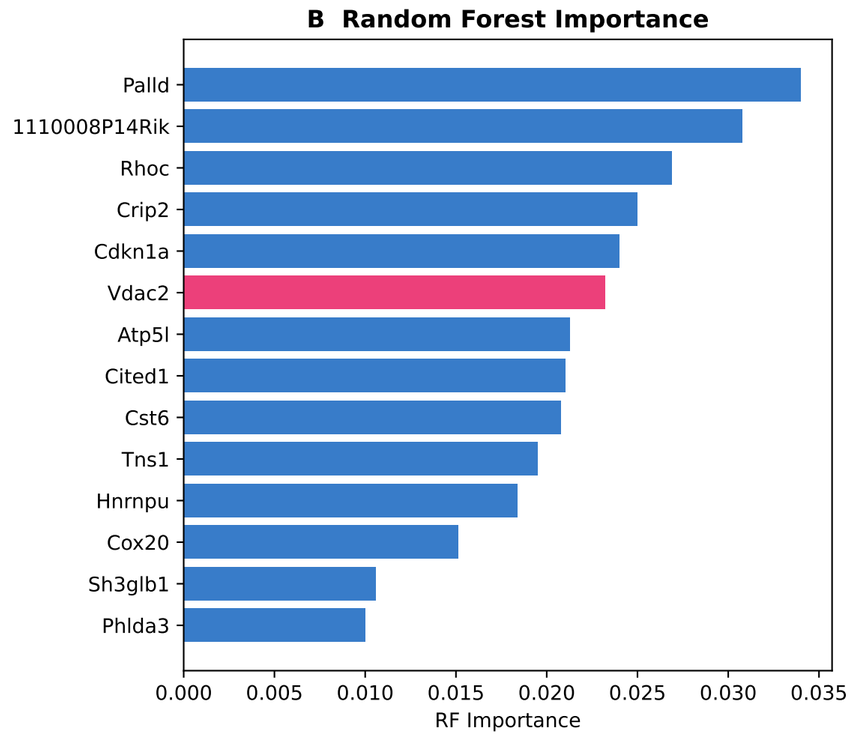

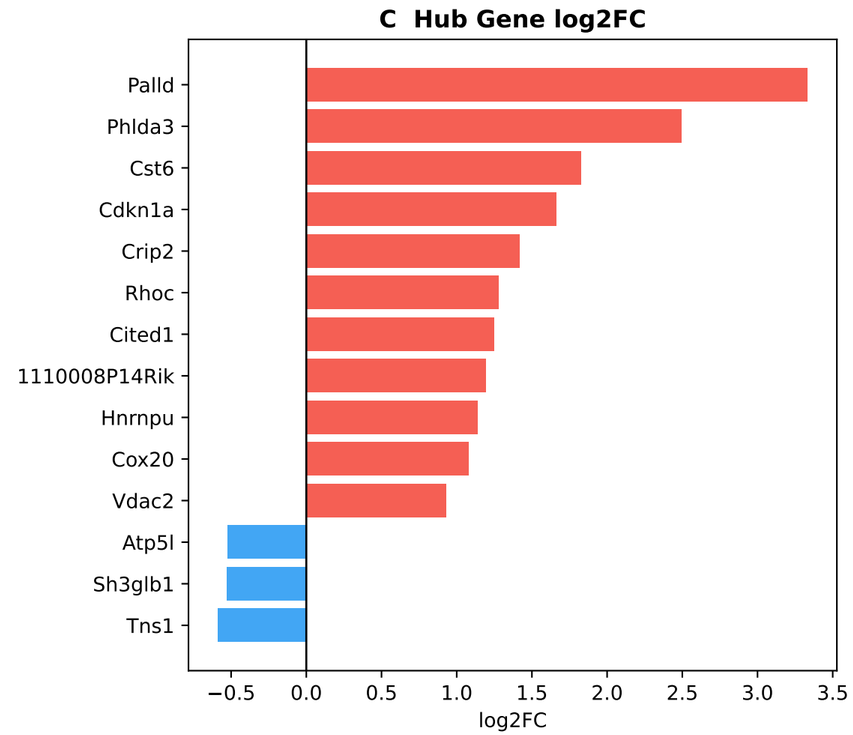

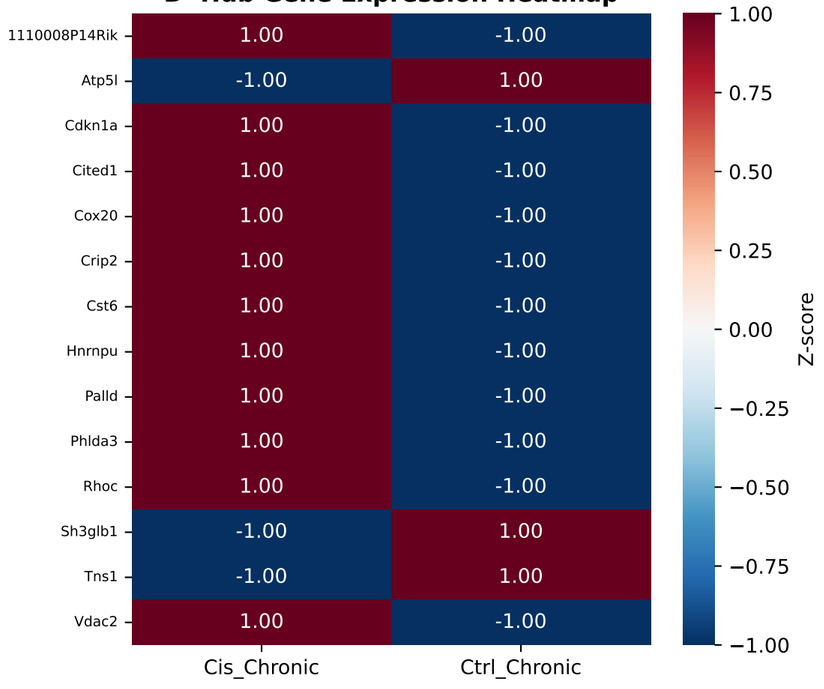

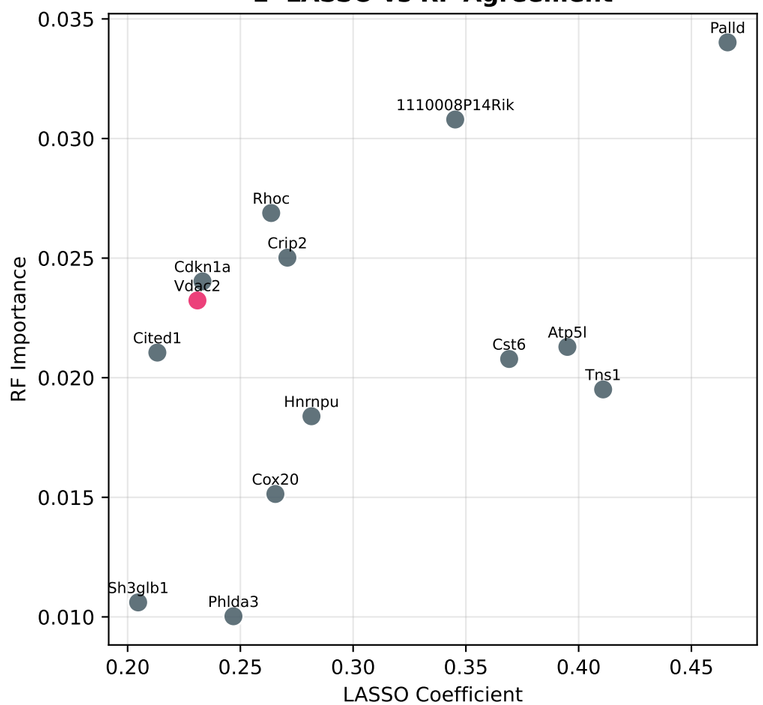

F Hub Gene Table

Gene	log2FC	padj	LASSO	RF
1110008P14Rik	1.19	2.3e-33	0.345	0.031
Atp5l	-0.52	2.9e-27	0.395	0.021
Cdkn1a	1.66	1.4e-27	0.233	0.024
Cited1	1.25	3.9e-28	0.213	0.021
Cox20	1.08	1.5e-21	0.266	0.015
Crip2	1.42	9.6e-28	0.271	0.025
Cst6	1.82	8.9e-26	0.369	0.021
Hnrnpu	1.14	2.9e-26	0.282	0.018
Palld	3.33	7.4e-25	0.466	0.034
Phlda3	2.5	1.0e-13	0.247	0.01
Rhoc	1.28	3.2e-32	0.264	0.027
Sh3glb1	-0.53	3.1e-03	0.205	0.011
Tns1	-0.59	3.2e-08	0.411	0.02
Vdac2	0.93	2.9e-26	0.231	0.023

Figure 6: WGCNA Module Analysis and Hub Gene Integration

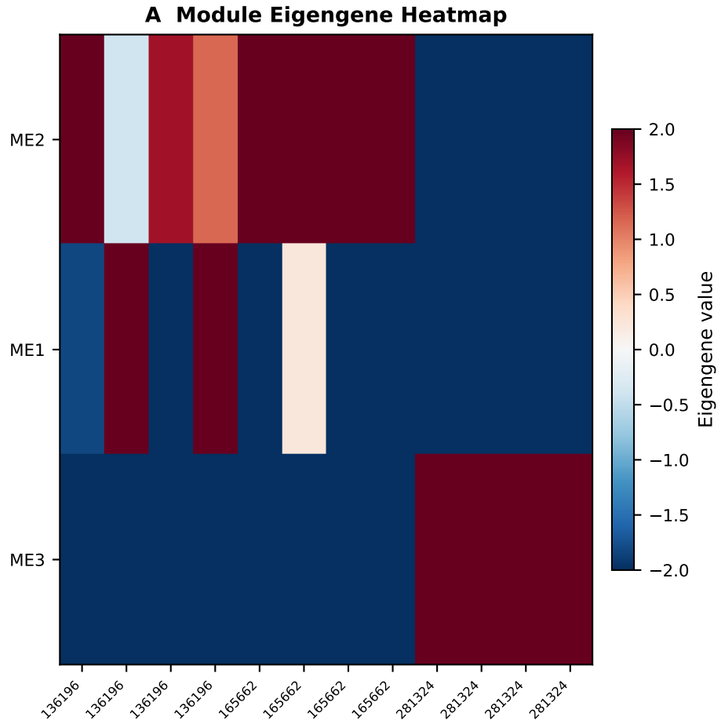

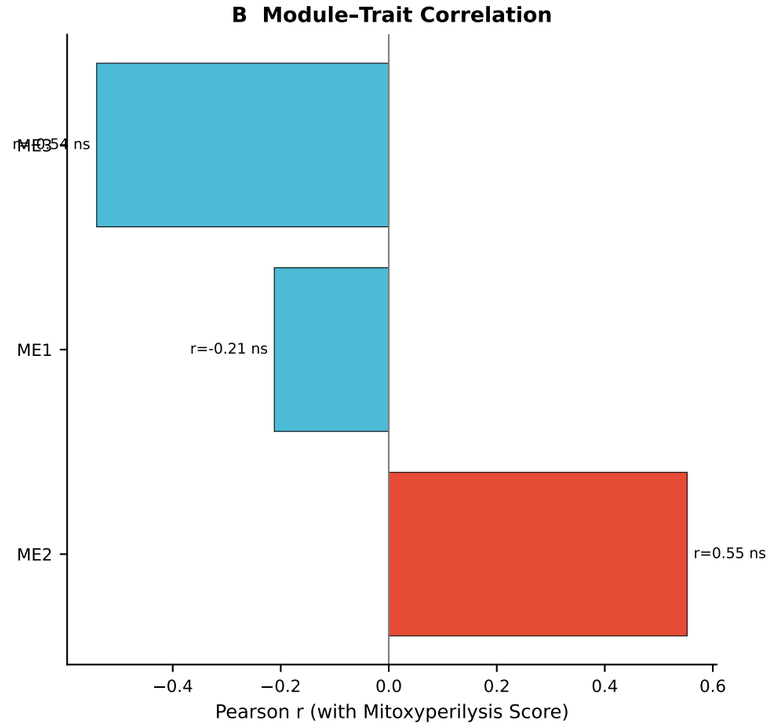

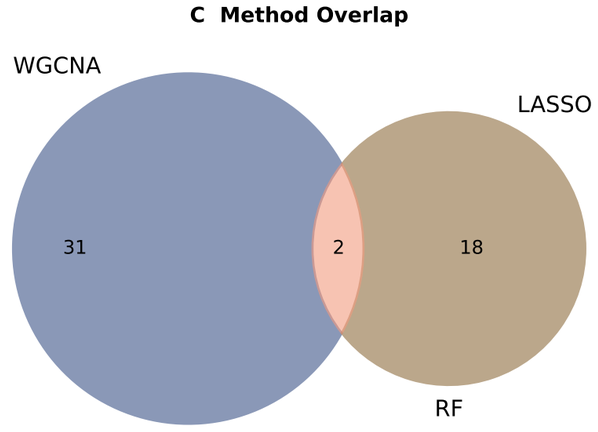

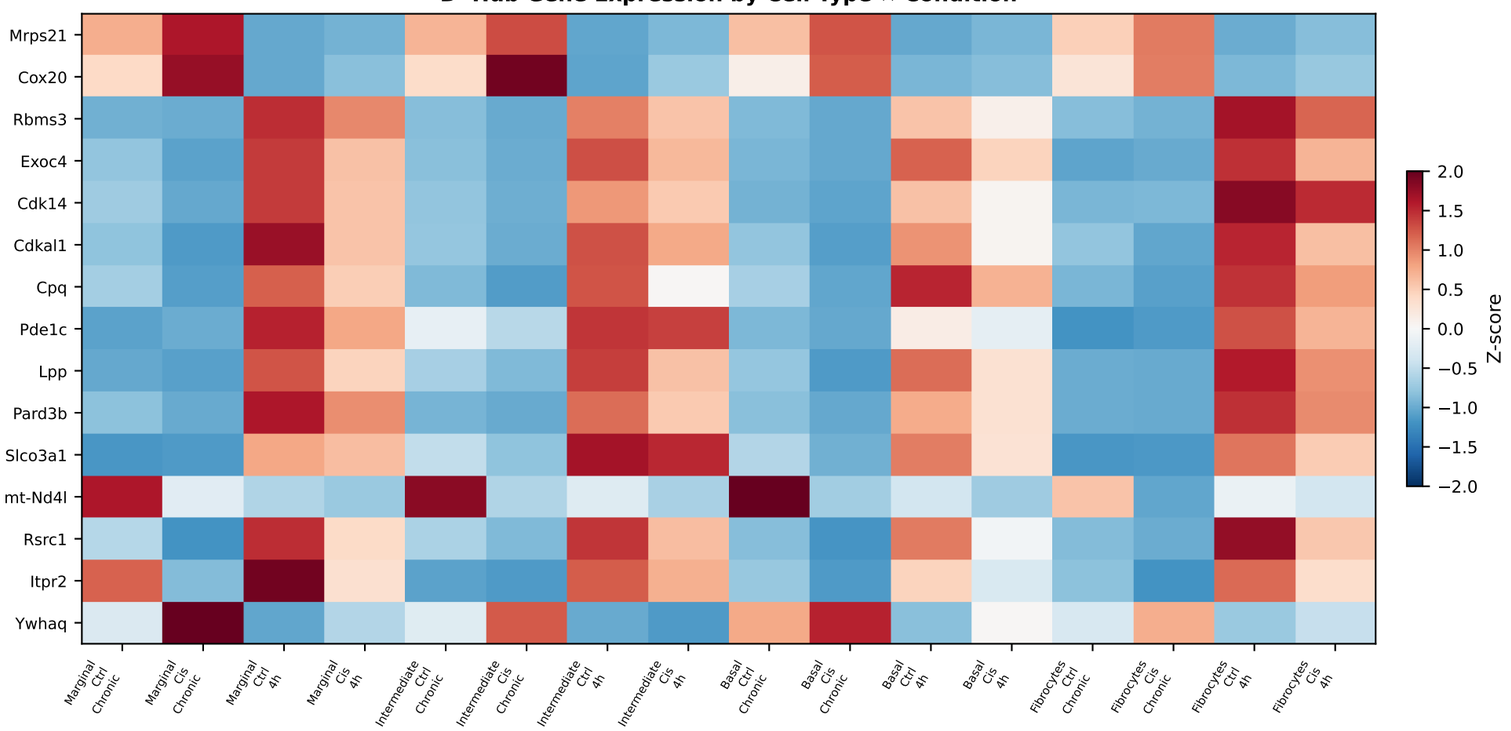

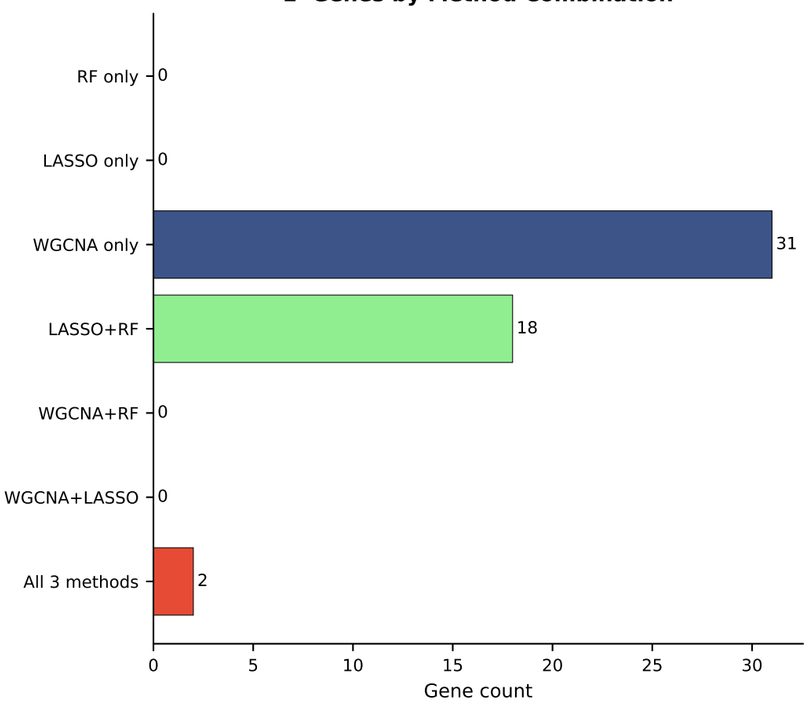

Figure 7: Hub Gene Prognostic Model

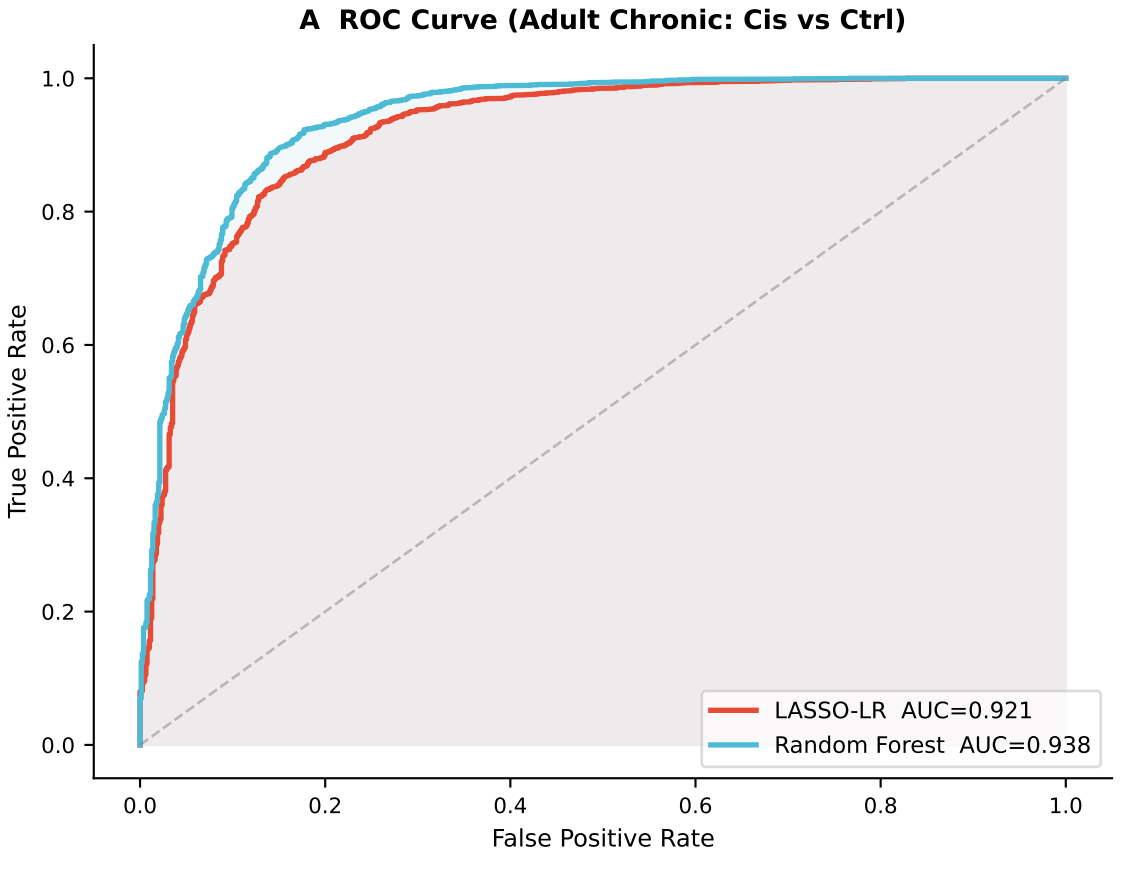

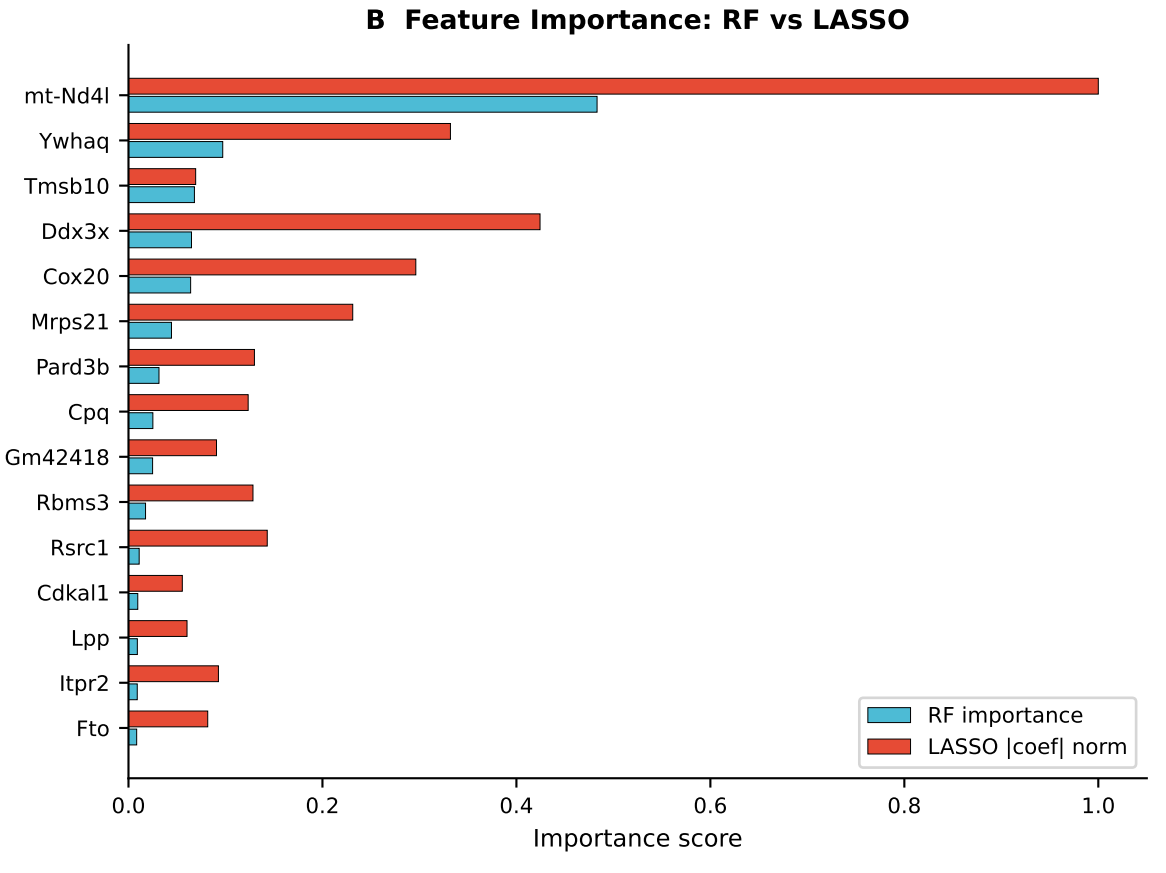

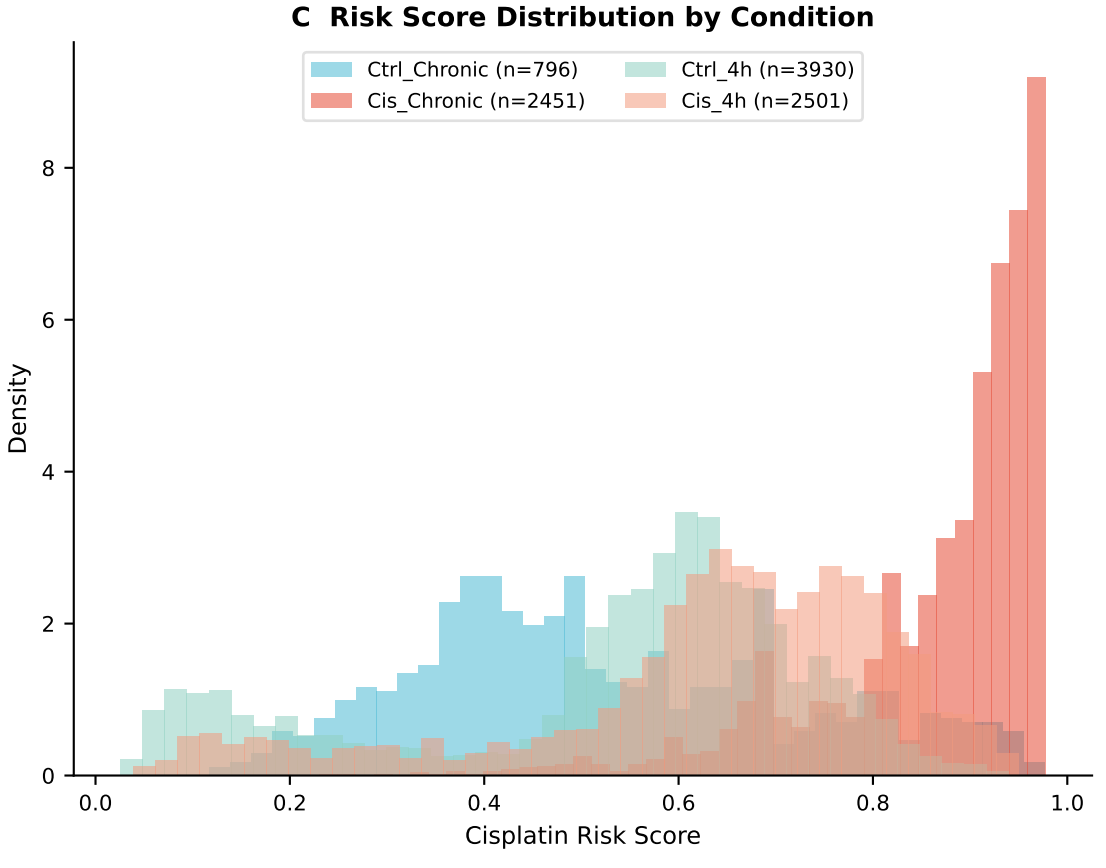

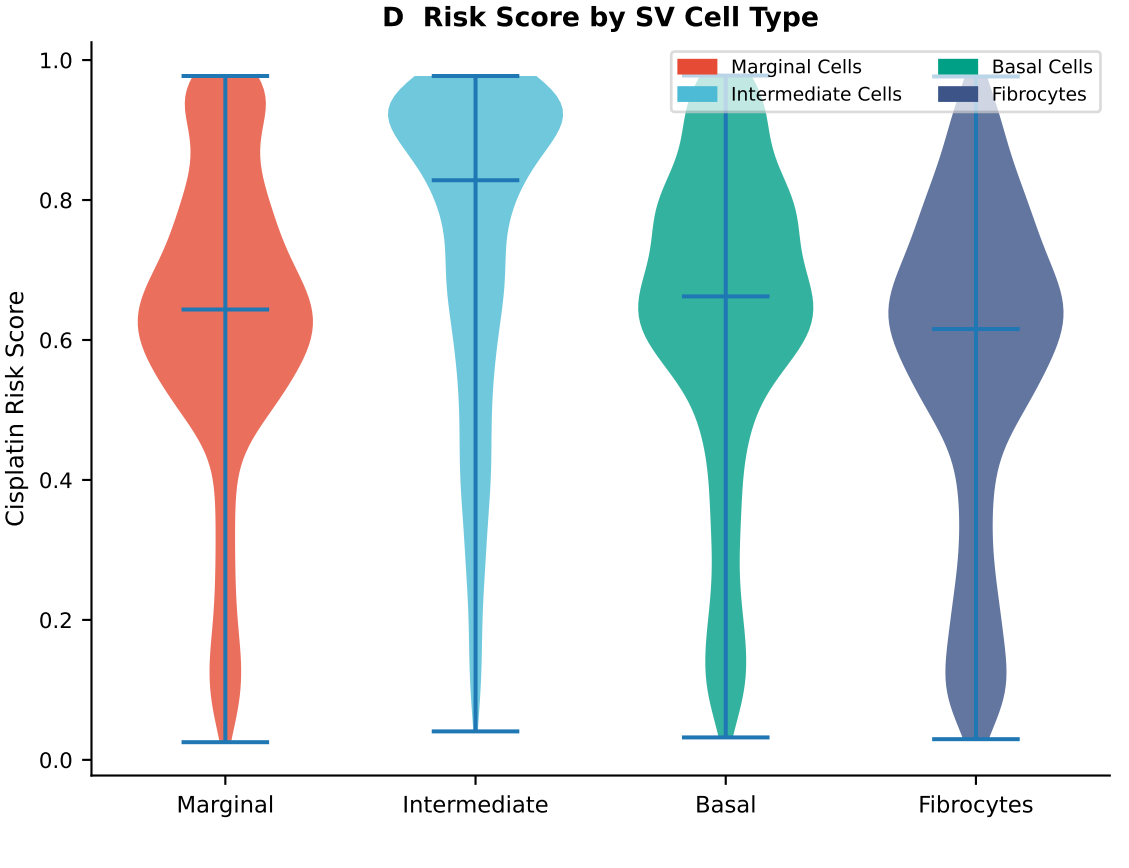

Figure 8: Hub Gene Expression in SV Cell Subpopulations

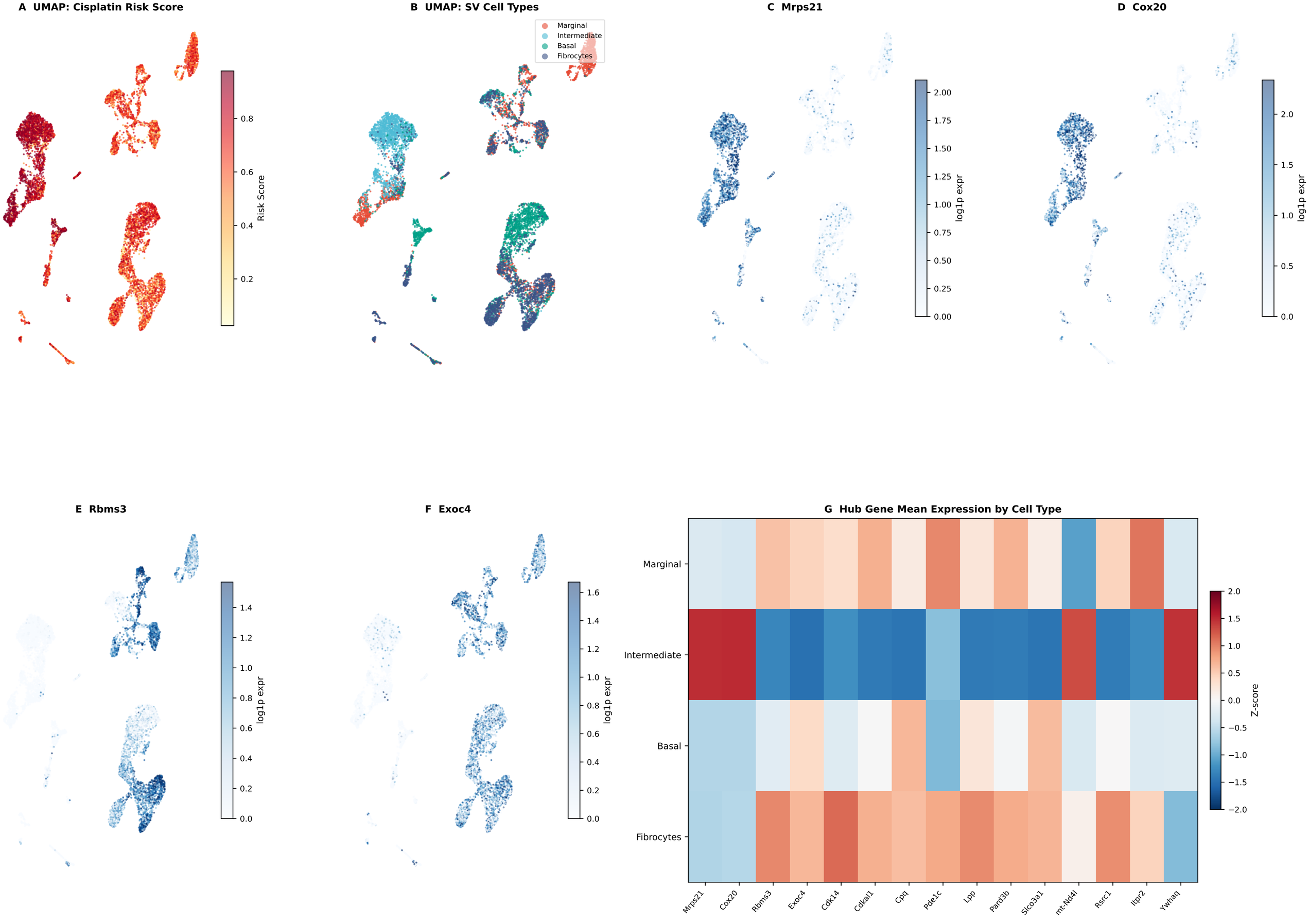

Figure 9: Network Pharmacology – Hub Gene Drug Targets

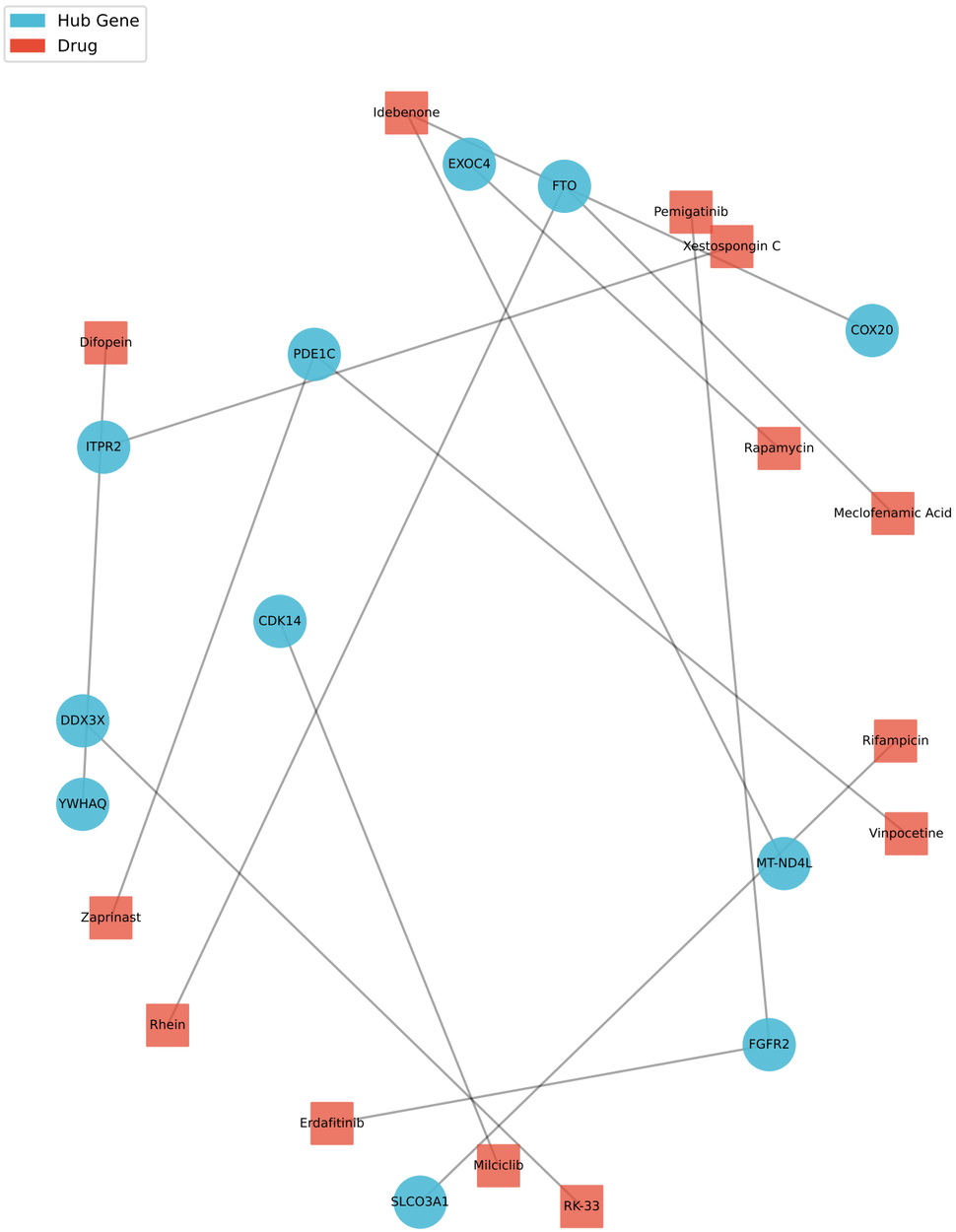

Figure 10. MD Simulation and Molecular Docking Analysis of mt-ND4L

A Backbone RMSD

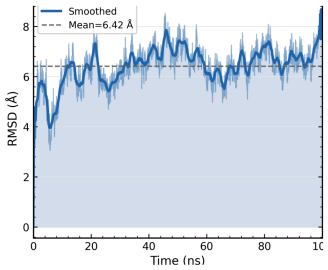

B Per-residue RMSF

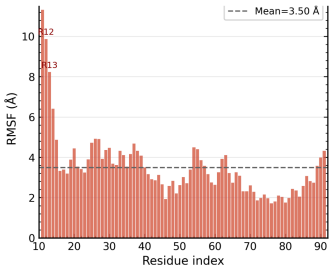

C Radius of Gyration

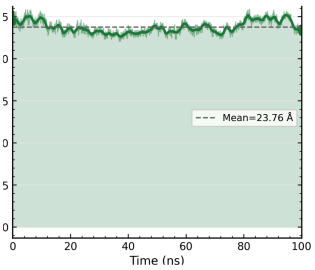

D Potential Energy

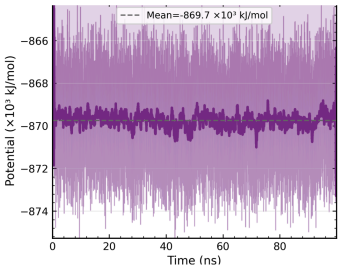

E Protein–POPC H-bonds

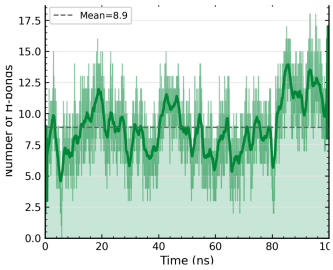

F Simulation Statistics

Parameter	Mean ± SD
RMSD (Å)	6.42 ± 0.83
RMSF (Å)	3.50 ± 1.56
Rg (Å)	23.76 ± 0.75
Potential (×10³ kJ/mol)	-869.7 ± 1.4
Protein–POPC H-bonds	8.9 ± 2.6

G

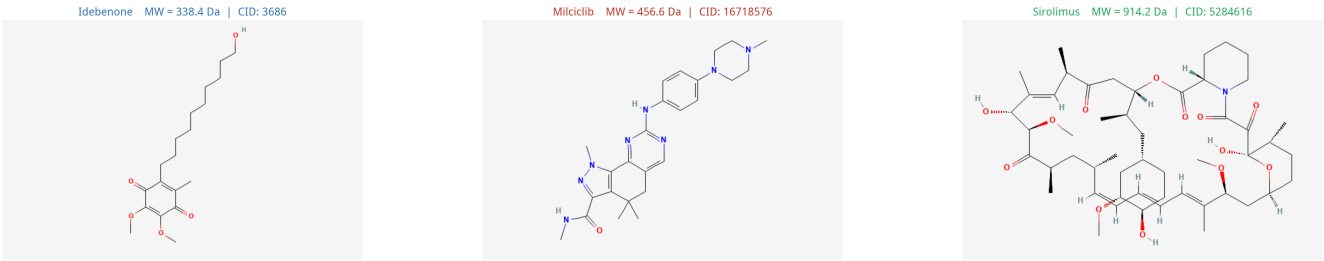

H

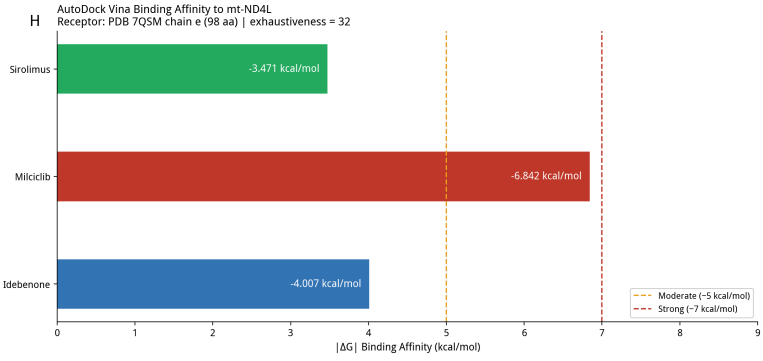

I Top-5 Pose Energies

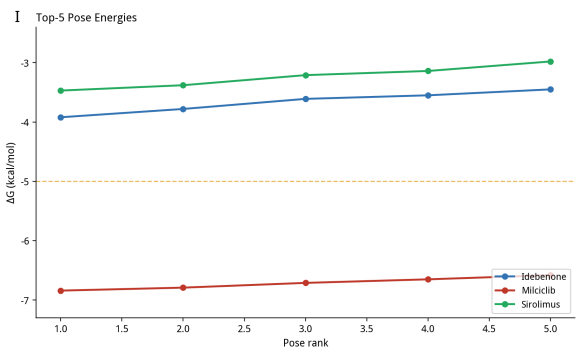

J Docking Summary & Scientific Interpretation

Compound	MW (Da)	Best ΔG (kcal/mol)	Mean ΔG (kcal/mol)	Strength	Mechanistic Interpretation
Idebenone	338.4	−4.007	−3.843	Weak	Vit K antioxidant; indirect via membrane
Milciclib	456.6	−6.842	−6.754	Moderate	CDK→Cdc42/Bax; moderate mt-ND4L
Sirolimus	914.2	−3.471	−3.267	Large Macrolide	mTORC2/Vdac2; steric exclusion

K Mechanistic Pathway